NASA TM X-490

TECHNICAL MEMORANDUM

X-490

HEAT-SHIELD PERFORMANCE DURING ATMOSPHERIC ENTRY OF PROJECT MERCURY RESEARCH AND DEVELOPMENT VEHICLE

By Robert L. O'Neal and Leonard Rabb

Space Task Group
Langley Field, Va.

NATIONAL AERONAUTICS AND SPACE ADMINISTRATION
WASHINGTON
May 1961

1J

NATIONAL AERONAUTICS AND SPACE ADMINISTRATION

TECHNICAL MEMORANDUM X-490

HEAT-SHIELD PERFORMANCE DURING ATMOSPHERIC ENTRY OF PROJECT MERCURY RESEARCH AND DEVELOPMENT VEHICLE*

By Robert L. O'Neal and Leonard Rabb

SUMMARY

A Project Mercury research and development vehicle has been flight tested to obtain atmospheric entry data on various concepts being employed in the Project Mercury vehicle design. One of the primary objectives of the test was to obtain performance data from the ablation heat shield during atmospheric-entry heating. The test proved the ablation heat shield to be an efficient and reliable heat protective device. Measured heat-shield temperatures and char depths indicated that the heat shield essentially experienced a uniform heating over its surface. The experimental heat load to the heat shield agreed well with that predicted by theory and indicated that surface reradiation and ablation dissipated approximately 75 percent of the total heat load.

INTRODUCTION

To give man the capability of earth orbital flight requires the development and qualification of new flight and vehicle-design concepts. One phase of orbital flight which has a marked influence on the design of a manned vehicle is that of entry into the earth's atmosphere. It is in this region that the high energy level of the vehicle is transformed into heat, offering a serious potential hazard. Efficient dissipation of this heat is necessary to preserve the structural integrity of the vehicle and its operational capability. For this purpose, the Mercury capsule design specifies the use of an ablation heat shield on its blunt face.

In the early stages of Project Mercury it was believed that a flight test was necessary to investigate concepts being used in the capsule design. This flight test was planned to simulate as nearly as possible the conditions of atmospheric entry from a shallow earth orbit of a full-scale capsule. This capsule was equipped with an ablation

heat shield made of a phenolic fiber glass resin material of the type planned for the Mercury heat shield and was instrumented so that its performance details could be determined. This was one of the primary objectives of the flight test.

The capsule (given the code name "Big Joe") flight test was conducted September 9, 1959, from the Air Force Missile Test Center, Cape Canaveral, Florida. This report presents the results of the ablation-heat-shield performance during this test.

SYMBOLS

c_w	specific heat of heat-shield material, Btu/lb-$^{\circ}$F
H_a	enthalpy of gas injected into boundary layer, Btu/lb
H_o	free-stream total enthalpy, Btu/lb
H_s	enthalpy of air evaluated at heat-shield surface temperature and stagnation pressure, Btu/lb
k	thermal conductivity of heat-shield material, Btu-ft/(sq ft)(sec)($^{\circ}$F)
L	latent heat of decomposition, Btu/lb
l	distance from heat-shield center to edge, ft
$\dot{m}$	rate of mass injection into boundary layer, lb/sec
Q	heat load per unit area, Btu/sq ft
q	heating rate, Btu/sq ft-sec
R_l	local Reynolds number at heat-shield corner
r	radial distance from geometric center of heat shield, in.
T	temperature, $^{\circ}$F
T_s	heat-shield surface temperature, $^{\circ}$F
t	time from 2-inch lift-off, sec

V	velocity relative to atmosphere, ft/sec
x	depth in heat shield measured perpendicular to outside surface, in.
α	thermal diffusivity, $k/\rho_w c_w$
β	transpiration efficiency factor, $\frac{H_a}{H_o - H_s}$
γ	relative flight-path angle referenced to local horizon, deg
ϵ	emissivity
ρ_w	density of heat-shield material, 108 lb/cu ft
σ	Stefan-Boltzmann constant, Btu/(sec)(sq ft)($^\circ$F abs)^4

CAPSULE DESCRIPTION

The test capsule had essentially the same external dimensions as the Mercury capsule with the exception that it was not fitted with an escape tower. Structural details of the capsule were not typical of the Mercury capsule as it was designed only to meet the requirements of this flight test. A sketch showing the general dimensions of the capsule is given in figure 1. The capsule is considered to consist of the following four major assemblies:

(1) Heat shield

(2) Pressurized instrumentation compartment

(3) Conical and cylindrical afterbody

(4) Aft canister

A photograph of the assembled capsule is shown in figure 2.

The heat shield was an ablative type made of phenolic resin and fiber glass and the afterbody was made of Inconel sheet. The capsule instrumentation was contained in the pressurized compartment and the parachute system and some recovery aids were contained in the afterbody and aft canister sections.

The heat shield used on the capsule was supplied by the General Electric Company and the B. F. Goodrich Company. The heat shield was geometrically a 74.5-inch-diameter spherical segment with a radius of curvature of 80 inches. A sketch of the heat shield is shown in figure 3. The heat shield consisted of two laminates, an ablation laminate 1.075 inches thick and an inner structural laminate 0.550 inch thick. The ablation laminate was made of concentric layers of fiber-glass cloth orientated so the layers were at a 20° angle with the local heat-shield surface. The structural laminate was made of fiber-glass cloth orientated with the individual layers parallel to the outer surface. Both the ablation and structural laminates were made from a Volan A finish fiber-glass cloth with a 91LD resin. Resin content, by weight, of the ablation and structural laminates was 40 percent and 30 percent, respectively. A circular ring (see fig. 3) 3 inches high, made of fiber glass and resin, was attached to the back of the heat shield and served to bolt the heat shield to the pressurized compartment of the capsule. A photograph of the completed heat shield is shown in figure 4.

HEAT-SHIELD INSTRUMENTATION

The ablation heat shield was instrumented to obtain temperature and char-penetration time histories during flight. Unique sensors were specifically developed to meet the requirements of the Space Task Group by the Missile and Space Vehicle Department of the General Electric Company, Philadelphia, Pennsylvania. The heat shield was instrumented with 13 of these sensors located at the positions indicated in table I. Each of the sensors consisted of two distinct types of measurements: first, six thermocouples spaced in depth as shown in table I and second, the char sensor circuits which consisted of 20 pairs of wires spaced in depth to form a single data intelligence. The individual pairs of wires utilized the property of the resin becoming an electrical conductor when charred to complete the electrical circuit between adjacent wires.

Part of the thermocouples in several sensors could not be used due to the limited number of commutator spaces available for telemetering. Three of the available six thermocouples were used in nine of the sensors, and all six thermocouples in each of the remaining four sensors were used. The individual thermocouples consisted of coaxial chromel-alumel wires insulated from each other and welded together at the hot junction.

The make wires and thermocouples were bonded to the surface of two small separate slabs made of the same material as the heat shield. The instrumented faces of the slabs were then bonded together with a small

spacer inserted between the make-wire and thermocouple circuits. Each sensor assembly was machined in the form of a plug and bonded in the desired location in the heat shield. The sensor assembly is illustrated schematically in the following sketch:

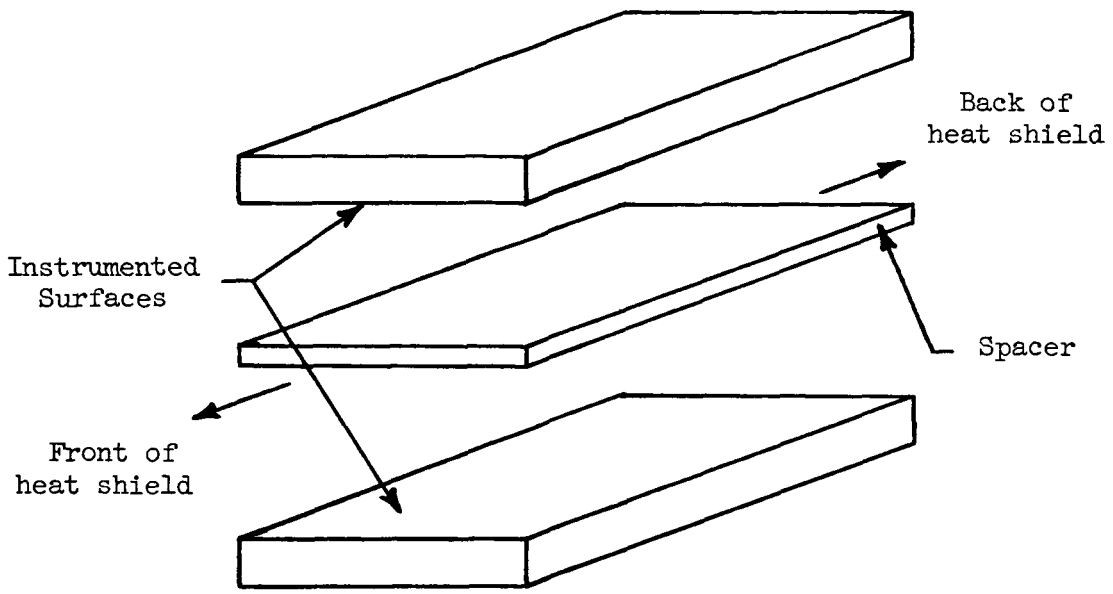

A back view of the heat shield (fig. 5) shows the leads used to connect the sensor instrumentation to the telemeter system. The grids noted in figure 5 are plastic strips used to insure close contact with the supporting structure.

The 51 thermocouples used in the heat shield were commutated on a single telemeter channel by means of a 60-point switch. The switching rate was such that each thermocouple was sampled about once every 0.62 second. Included with the data during each cycle of the switching motor was a master identification pulse as well as calibrate signals consisting of low, medium, and high values of the preselected thermocouple temperature range. These calibrate signals provided continuous in-flight calibration of the thermocouple system. The maximum temperature of the preselected range for the thermocouples was approximately 2,600° F.

The outputs from the 13 char sensors were also commutated on a single telemeter channel. In this case, a 30-point switch was used

with a sampling rate such that each char sensor was sampled at least once during approximately every 0.40 second with some sensors being sampled twice within this time interval. Continuous in-flight calibration of the char sensors was obtained by including signals representing minimum and maximum output voltages from these sensors.

The capsule was instrumented with three FM/FM, 20-watt RF links which transmitted the data measurements to ground receiving stations. One link transmitted primary data, including heat-shield performance, and a second link transmitted secondary data. The third link also transmitted primary data to obtain added reliability and was intended to rebroadcast primary link data which was onboard recorded during ionization blackout of the telemetry signal; however, the playback system did not function and the data was not rebroadcast. Two tape recorders were used to provide an onboard data source by recording all primary link data. These recorders were programed to cover the entire period of flight. A photograph of the instrumentation contained in the pressurized compartment is shown in figure 6.

The capsule was equipped with both S-band and C-band radar beacons to aid in tracking the capsule during entry into the earth's atmosphere. The antennas used for the beacon system and telemetry system are shown in figure 2. Trajectory data were not obtained during entry; therefore, the use of an estimated trajectory was required as described in a subsequent section.

DATA REDUCTION

The heat-shield temperatures were obtained by using both telemetered and onboard-recorded data. Telemetered data were not available during the time range from approximately 480 to 580 seconds due to the telemetry blackout. Data from onboard recorders were used during this time interval. Faired values of the measured heat-shield temperatures are shown in figure 7, grouped according to sensor number. Figure 8 shows the data points used to obtain such a fairing for a typical thermocouple. It is seen that, in general, the readings were within $\pm 50^{\circ}$ F of the faired curve. This represents approximately ± 2 percent of the full-scale calibrated temperature range which is believed to be the order of accuracy of the data.

In order to evaluate the performance of the heat shield properly, it was necessary to calculate the heat-shield surface temperature. This was done by using temperature profiles obtained near the heat-shield surface from the measured temperatures. The region of the heat

shield near the outside surface was analytically divided into small elements as shown in the following sketch:

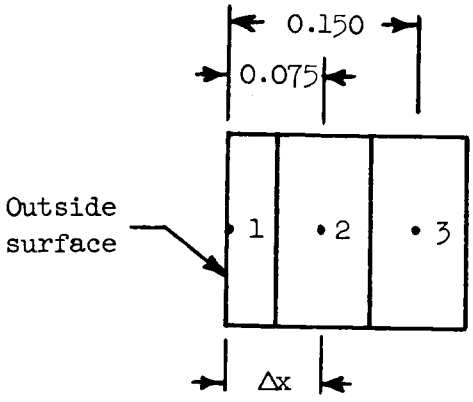

The following heat-balance equation was written for element 2:

$$\frac{\Delta T_2}{\Delta t} = \frac{k}{\rho_w c_w (\Delta x)^2} \left(T_1 - 2T_2 + T_3 \right)$$

As the temperature-time history of elements 2 and 3 are known from the heat-shield-temperature distribution, the surface temperature can be calculated from the relation

$$T_1 = \left(\frac{\Delta T_2}{\Delta t} \right) \frac{(\Delta x)^2 \rho_w c_w}{k} + 2T_2 - T_3$$

Since the thermal diffusivity α is equal to $k/\rho_w c_w$, the preceding equation can be expressed

$$T_1 = \left(\frac{\Delta T_2}{\Delta t} \right) \frac{(\Delta x)^2}{\alpha} + 2T_2 - T_3$$

Information furnished by the heat-shield contractor concerning material properties indicated that the diffusivity remained relatively unchanged by the charring process.

Figure 9 shows the surface temperature obtained by this method. The material and thermal properties were assumed to be constant with the following values:

ρ_w = 108 lb/cu ft

k = 6.75×10^{-5} Btu-ft/(sq ft)(sec)($^\circ$F)

c_w = 0.265 Btu/lb-$^\circ$F

The calculated surface temperature was used to compute the heat lost by radiation with a surface emissivity of 0.80 assumed. (See section entitled "Heating Rate.") A check was made to determine the confidence level of the computed surface temperature by comparing the heat absorbed throughout the shield with the computed value of $k \frac{\partial T}{\partial x}$ at the surface. The value of $k \frac{\partial T}{\partial x}$ was within 10 percent of the heat absorbed.

FLIGHT DESCRIPTION

The booster used for this flight test was the Atlas 10D missile. The capsule was attached to the capsule-booster adapter by means of a Marman clamp. Figure 10 shows a photograph of the capsule and booster combination on the launch stand.

The missile was launched at 2:19 a.m. e.s.t. on September 9, 1959, from the Air Force Missile Test Center, Cape Canaveral, Florida. A malfunction occurred during the boost phase in that the booster engine did not separate from the Atlas after burnout. This added weight caused the insertion conditions at sustainer-engine burnout to be different than would normally be obtained. This malfunction also led to a delay in separation of the capsule from the Atlas after Marman band release. After separation, the capsule attained a heat-shield-forward attitude which it maintained throughout entry into the earth's atmosphere. The capsule coordinates in space near apogee as obtained from radar data were used in conjunction with onboard-recorded loads data to calculate the entry trajectory. The accuracy of the trajectory determined by this technique is affected by uncertainties in various parameters in the calculations, such as capsule drag coefficient and air density. By varying these parameters over what appeared to be a reasonable range, it was possible to obtain a trajectory which closely approximated the measured capsule loads. The nominal trajectory calculated is shown in figure 11.

The capsule was equipped with an automatic reaction control system to control its motion during entry. However, due to the delay in capsule-booster separation, the control-system fuel supply was expended in attempting to control the motion of the capsule-booster combination. Data concerning the capsule motion during entry indicated that the capsule was oscillating about a trim angle of about 4° or less. The average amplitude of this oscillation about the trim angle over the time interval of interest in the analysis of the heat-shield performance was of the order of 12° to 15°. This trim angle was caused by the capsule center of gravity being offset from its longitudinal axis.

The parachute landing system of the capsule operated successfully, resulting in a safe water landing. The recovery aids enabled location of the capsule and it was recovered in excellent condition 7 hours after launch.

RESULTS AND DISCUSSION

The desired insertion conditions for this flight test were intended to simulate closely atmospheric entry from a shallow earth orbit. However, due to the failure of the booster engine to separate from the Atlas, the heating environment of the heat shield was not as severe as would have occurred had the desired trajectory been obtained. A comparison was made by use of the theory of Detra, Kemp, and Riddell (ref. 1), of the heating obtained from the present flight test and that estimated for the anticipated flight. This comparison of values (fig. 12), based on zero wall enthalpy, showed the peak heating rate obtained during the flight to be approximately 77 percent of the desired value and the total heat load obtained to be approximately 42 percent of the desired value of 7,100 Btu/sq ft.

An evaluation of the heat-shield performance involves analysis of the test results with regard to several important categories. The categories chosen as being necessary to describe the performance adequately are:

(1) General condition of the recovered heat shield

(2) Heat-shield temperatures and char characteristics

(3) Heat-shield heating rate and mechanisms of ablation

Each of these items is discussed in detail in the following sections.

Description of Recovered Heat Shield

The ablation heat shield withstood the rigors of both the entry and recovery phases of the flight test with only superficial damage.

A photograph (fig. 13) shows the recovered heat shield. The pie-shaped discolored region visible in quadrant II was caused by a dye-marker recovery aid and was not due to any effects of heating. The random dark marks are scuff marks made during the capsule recovery operation. A closeup view of a section of the heat shield is shown in figure 14. Small droplets of fused glass, typical of the entire heat-shield surface, are clearly visible. An offset stagnation point of approximately 6 inches due to the trim angle was evident from the streamlined glass droplets. Also visible are small circumferential

hairline cracks which follow the fiber-glass laminations. The only significant damage to the heat shield was a 3-inch delamination which occurred in quadrant III near the stagnation point as shown in figure 15. Also seen in this figure is a crack at the edge of the large center plug and a separation around the smaller center plug. It was found by sectioning the heat shield at appropriate locations that all cracks and delaminations in the heat shield did not extend in depth beyond the visible charred portion and did not affect the structural integrity of the heat shield. This can be seen for the case of the small center plug in figure 16 where the separation shown extends to a depth of approximately 0.2 inch.

Measurements were made of the heat-shield profile and thickness after recovery to determine if there was a change as a result of the flight test. The results indicated that any profile change which might have occurred was within the accuracy of the measurements ($\pm$0.01 inch). The heat shield was weighed after recovery and the results indicated a weight loss of 6 pounds. A more precise evaluation of the weight loss as a result of the flight test will be discussed in a later section.

Heat-Shield Temperatures and Char Characteristics

Heat-shield temperatures.- It was found by comparing temperatures from the different sensors that there was no significant effect of radial location on the heat-shield temperatures. This agreement can be seen in figure 17 where at a time near peak heating the temperature distribution through the heat shield is shown by use of the data from all sensors. This agreement was equally good at other times, an indication that the heat shield essentially experienced a uniform heating over its surface. The thermal analysis of the heat shield was made from average temperature profiles obtained by using all measured temperatures together at each time similar to that shown in figure 17. The temperatures obtained from these distributions at depths of $x = 0.075$ inch and $x = 0.150$ inch were used in calculating the surface temperature as described in the section entitled "Data Reduction." Temperature profiles through the heat shield at various times are shown in figure 18. It is seen that large temperature gradients exist in the heat shield as late as 600 seconds, the approximate time at which the aerodynamic heating becomes negligible. The envelope of the temperature distributions, that is, the maximum temperature reached at each point in the heat shield by 680 seconds, is shown in figure 19. It can be seen that, even though the calculated surface temperature reached values as high as 2,245° F, the internal temperature did not exceed 330° F at a depth of 0.40 inch. The temperature curve of figure 19 is slightly low at depths greater than 0.40 inch because internal heating by conduction was indicated for times greater than 680 seconds.

Char characteristics.- Core samples were taken from the recovered heat shield at various locations on its surface to obtain evidence of its physical condition. Figure 20 shows a photograph of the samples removed from the heat shield. It was found by measurements of these samples that a visible charred region penetrated to a depth of approximately 0.20 inch and an additional discolored region extended to a total depth of approximately 0.35 inch.

As a means of obtaining a better understanding of the extent of the char rather than arbitrarily defining char visually, specimens of the heat shield were tested to obtain its electrical resistance and specific-gravity properties. The electrical resistance of a typical core sample cut from the heat shield was measured at regular intervals from its front face with the results shown in figure 21. It is seen that there is a definite transition at a depth of about 0.12 inch with the outer portion being electrically conductive while the interior retains its original property as a dielectric. Specific-gravity measurements were made from sections cut from one of the heat-shield core samples (number 13). Sections representative of the electrically conductive portion, the remainder of the visual char, the discolored region, and virgin material were used to obtain the variation of specific gravity with depth. The results of these specific-gravity measurements are presented in figure 22. It is seen that the decrease in specific gravity is not confined to the visible char region but exists in varying degrees to a depth of about 0.40 inch. It was assumed that the specific gravity of the electrically conductive region was a constant value of 1.55. This indicates that the region extending to a depth of approximately 0.12 inch lost approximately 25 percent of its original resin content. The results of the specific-gravity tests roughly confirm the char depth as indicated from electrical-resistance measurements (0.12 inch) rather than 0.20 inch as indicated by visual inspection. These tests also indicate three distinct regions which reflect the results of the entry heating and are defined as follows along with the general range in depth in the heat shield at which they exist:

(1)	Char	x = 0 to 0.12
(2)	Visible char	x = 0.12 to 0.20
(3)	Discolored region	x = 0.20 to 0.35

From the maximum-temperature-penetration curve, (fig. 19) it is seen that the char and visible-char phenomena occur at temperatures of approximately 1,000° F and 600° F, respectively. The extent of these regions below the heat-shield surface is indicated on the photograph of the stagnation-point sensor shown in figure 16.

During this flight test the heating rates were low enough so the ablation process was confined to charring the resin portion of the

heat shield with no surface recession. The char sensors were calibrated to indicate the progression of the char front. This calibration was obtained from ground tests conducted by the heat-shield contractor by use of sensor-instrumented models. The results obtained from the sensor readings during this flight test were satisfactory in a qualitative sense but indicated excessive char depths ranging from 0.275 inch to 0.365 inch as compared to the actual value of about 0.12 inch. This is attributed to difficulties associated with a proper calibration of the system.

The distribution of the visible-char and discolored-region penetration levels measured from the heat-shield samples are shown in figure 23(a). The sketch in the same figure shows the relative locations of the points on the shield where the samples were removed. It can be seen that the maximum visible-char penetration is 0.21 inch at the heat-shield center and decreases slightly with radial distance to a minimum of about 0.19 inch, representing a variation of approximately 10 percent. The discolored region also reached its maximum penetration of about 0.38 inch near the heat-shield center. This depth decreased to a value of about 0.31 inch at a radial distance of 8 inches and increased to a value of about 0.34 inch at points nearer the edges of the heat shield. Visible-char and discolored-region depths obtained from plugs taken at various angular positions around the heat shield at a radius of 33.5 inches is shown in figure 23(b). It is evident that there was no significant effect of angular position on the depth of penetration of either of these phenomena. A sample cut from the extreme edge of the heat shield showed the visible-char penetration level to be essentially the same as noted at other points over the heat shield. The data of reference 2 for a nose shape similar to the present heat shield indicates a heating rate near the extreme edge approximately 15 percent greater than exists at the stagnation point. This appears to be a conservative value for the present test as no evidence of appreciable increased heating was in evidence. The uniformity of the visible-char depths over the heat shield, like the uniform temperature distribution, lends credence to the fact that the heat shield had essentially undergone a uniform heating.

Heating Rate

A comparison of the experimental and theoretical heating rates for the heat shield are shown in figure 24. The theoretical heating rate was obtained by use of the theory of Detra, Kemp, and Riddell (ref. 1) for the stagnation point of a sphere having an 80 inch radius and by use of the 1959 ARDC model atmosphere (ref. 3). The surface enthalpy was based on the calculated surface temperature shown in figure 9. The

experimental values were based on the measured temperatures within the heat shield plus the following assumptions:

(1) Surface emissivity, $\epsilon = 0.80$ (from contractor's tests)

(2) Transpiration efficiency factor, $\beta = 0.50$

The transpiration efficiency factor β is defined as $\beta = \frac{H_a}{H_o - H_s}$ where H_a is the enthalpy of the injected gas in the boundary layer and the term $H_o - H_s$ is the air enthalpy potential across the boundary layer. The efficiency factor β is a measure of the ability of the injected gas to block heat transfer from the boundary layer to the heat shield. The value of 0.50 used for β in this analysis is given in reference 4 as being representative of reinforced plastics of the type used in the present heat shield and ablating in the presence of a laminar boundary layer. It is felt that the boundary layer over the heat shield was laminar during the period of major heating as the maximum local Reynolds number, that existing at the heat-shield corner, did not exceed 0.50×10^6 until approximately 590 seconds. The local Reynolds number at the corner of the heat shield shown in figure 25 was calculated by assuming a Newtonian pressure distribution over the heat-shield surface.

The experimental heating-rate curve (fig. 24) is composed of the following three terms:

(1) Heat absorbed by the heat shield

(2) Surface radiation

(3) Heat absorbed in vaporizing the resin lost and the heat blocked by the gas injected into the boundary layer

Figure 26 presents the calculated time history of each of the three contributions to the heating rate to the heat shield. The method used to determine the magnitude of each contribution is described in the following paragraph.

The net heat absorbed by the heat shield as indicated by a change in temperature was determined by integration of the temperature distribution through the heat shield at frequent time intervals. At any one time the net heat absorbed is

$$Q = \int_0^x \rho_w c_w T \, dx$$

with the material density ρ_w and specific heat c_w being assumed constant. By differentiating the time variation of the net heat absorbed, the rate at which heat was being absorbed was obtained. The heat lost by radiation at the heat-shield surface was calculated by the relation

$$q_{radiation} = \epsilon\sigma T_s^4 \quad \text{where} \quad T_s \quad \text{is} \quad {}^{\circ}\text{F abs}$$

The heat dissipated by the combined effect of the resin vaporization and blockage by the gas injected into the boundary layer was calculated by use of the appropriate part of equation (24) of reference 5. Using the definition of the transpiration efficiency factor discussed previously, equation (24) of reference 5 is equivalent to

$$q_{ablation} = \left[L + \beta\left(H_o - H_s\right) \right] \dot{m}$$

The heat capacity of the gas lost has been included in the term describing the heat absorbed by the heat shield. The value of the latent heat of decomposition L of the type of resin used in the heat shield is commonly accepted as 1,000 Btu per pound of resin. As the heat-shield weight analysis showed only 25 percent of the available resin in the char layer was lost as a gas, this indicated that it was necessary to decompose 4 pounds of resin to give 1 pound of gas. Therefore the latent heat of sublimation used was 4,000 Btu per pound of gas. The rate at which gas was injected into the boundary layer $\dot{m}$ is shown in figure 27, presented as the weight-loss rate of the heat shield. The limitations of the assumption used to determine the weight-loss rate are recognized. For example, the interdependence of $\dot{m}$ and time and temperature require a knowledge of the pyrolysis-rate equations from independent measurements. Attempts to make the analysis on the basis of weight-loss rate as a function of the transient temperature distributions were unsuccessful. The method used to determine the weight-loss rate (fig. 27) is discussed in the following paragraph.

The density variation measured at various depths in the recovered heat shield (fig. 22) indicated a weight loss variation with temperature. To obtain the heat-shield weight-loss rate shown in figure 27, it was assumed that attaining a certain temperature level at any point in the heat shield would result in an associated weight loss. The variation of density loss with temperature was obtained by correlating the specific gravity measured at depths in the heat shield with the maximum temperature attained by these points during the flight. This amounted to cross-plotting figures 19 and 22 with the results shown in figure 28. It is noted that the resin loss begins between 300° F and 400° F and the process is essentially completed at approximately 1,000° F. By using this density loss variation with temperature, the measured

temperature distributions through the heat shield were converted to density-loss distributions and integrated at regular time intervals to give the accumulative weight loss shown in figure 29. The total accumulative weight loss of 0.206 lb/sq ft represents a total of about 6.5 pounds for the entire heat shield which agrees well with the 6 pounds obtained by weighing the recovered heat shield. By differentiating the accumulative weight loss, the variation of weight-loss rate with time (fig. 27) was obtained.

The theoretical average heat input over the heat shield at angles of attack of the order encountered in this flight test would be of the order of 5 percent lower than the theoretical stagnation-point heat input of 2,610 Btu/sq ft shown in figure 24 if any edge heating effects were ignored. The result is a theoretical average heat input of approximately 2,500 Btu/sq ft, which, compared with the experimental average heat input of 2,795 Btu/sq ft (fig. 24), shows the agreement between the two to be of the order of 10 percent. This order of agreement is well within the accuracy of the experimental data and indicates that the values assumed for the latent heat of decomposition and transpiration efficiency factor were quite adequate. It is felt that the trajectory uncertainties mentioned previously could influence the aerodynamic heating rate predicted for the heat shield by the amount indicated by the hatched band of figure 30.

It can be seen in figure 26 that ablation and surface radiation represent 75 percent of the total heating to the heat shield. The large percentage of heat which was dissipated shows the advantage of combining high emissivity with good ablation performance. The quantity of heat dissipated by the ablation process shows the ability of small amounts of gas injection to absorb large amounts of heat. In this test a total mass loss of only 0.206 lb/sq ft gave a total heat rejection capacity of 1,350 Btu/sq ft. This corresponds to 6,550 Btu of heat consumed per pound of ejected gas.

SUMMARY OF RESULTS

A Project Mercury research and development vehicle has been flight tested to obtain data on various concepts being employed in the Project Mercury design. One of the primary objectives of the flight test was to obtain performance data from the ablation heat shield during atmospheric-entry heating. This phase of the flight test yielded the following results:

1. Although the trajectory flown by the test vehicle was different than that anticipated for a typical Mercury entry, the test proved that

the ablation heat shield was an efficient and reliable heat protective device. Not only did the heat shield demonstrate the ability to withstand the heating during entry with only minor surface delaminations, but it also showed no effects due to landing loads.

2. Measured heat-shield temperatures and char depths indicated that the heat shield essentially experienced a uniform heating over its surface. Specific-gravity measurements of the recovered heat shield indicated that in the charring process only 25 percent of the available resin content was lost.

3. The experimental heat load of the heat shield agreed well with that predicted by theory and indicated that surface reradiation and ablation dissipated approximately 75 percent of the total heat load.

Goddard Space Flight Center, Space Task Group,
National Aeronautics and Space Administration,
Langley Field, Va., October 12, 1960.

REFERENCES

1. Detra, R. W., Kemp, N. H., and Riddell, F. R.: Addendum to 'Heat Transfer to Satellite Vehicles Re-entering the Atmosphere.' Jet Propulsion, vol. 27, no. 12, Dec. 1957, pp. 1256-1257.

2. Stoney, William E., Jr.: Aerodynamic Heating of Blunt Nose Shapes at Mach Numbers up to 14. NACA RM L58E05a, 1958.

3. Minzner, R. A., Champion, K. S. W., and Pond, H. L.: The ARDC Model Atmosphere, 1959. Air Force Surveys in Geophysics No. 115 (AFCRC-TR-59-267), Air Force Cambridge Res. Center, Aug. 1959.

4. Scala, Sinclaire M.: A Study of Hypersonic Ablation. Tech. Inf. Series No. R59SD438 (Contract No. AF 04(647)-269), Missile and Space Vehicle Dept., Gen. Elec. Co., Sept. 30, 1959.

5. Roberts, Leonard: An Analysis of Ablation-Shield Requirements for Manned Reentry Vehicles. NASA TR R-62, 1960.

[redacted]

TABLE I.- HEAT-SHIELD INSTRUMENTATION

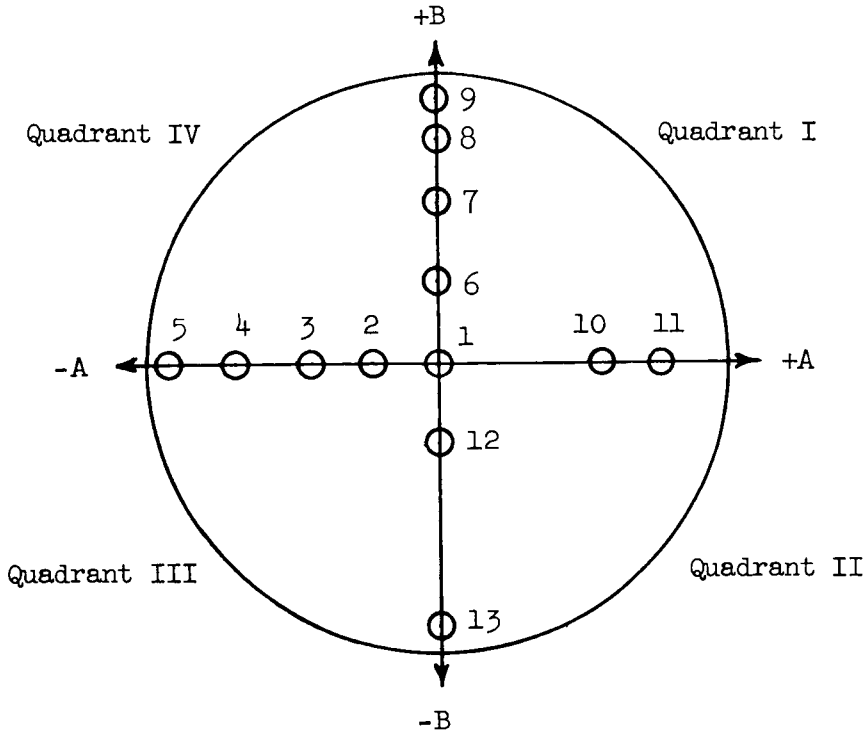

Sensor	Location		Thermocouple (a)	Depth from surface, in. (b)
	A, in.	B, in.		
1	0	0	1	0.067
			2	.187
			3	.347
			4	.677
			5	1.067
			6	1.607
2	-7.4	0	34	0.071
			35	.191
			36	.351
			37	.681
			38	1.071
			39	1.611
3	-14.8	0	7	0.085
			8	.365
			9	1.085

[a] All thermocouples were chromel-alumel.
[b] The accuracy of depth measurement is ±0.001 inch.

[redacted]

TABLE I.- HEAT-SHIELD INSTRUMENTATION - Concluded

Sensor	Location		Thermocouple	Depth from surface, in.
	A, in.	B, in.	(a)	(b)
4	-26.6	0	40	0.092
			41	.372
			42	1.092
5	-35.8	0	43	0.096
			44	.216
			45	.376
			46	.706
			47	1.096
			48	1.636
6	0	11.2	10	0.099
			11	.379
			12	1.099
7	0	21.6	49	0.086
			50	.206
			51	.366
			52	.696
			53	1.086
			54	1.626
8	0	29.2	13	0.080
			14	.360
			15	1.080
9	0	35.8	16	0.098
			17	.378
			18	1.098
			55	1.098
10	21.6	0	19	0.092
			20	.372
			21	1.092
11	29.2	0	22	0.099
			23	.379
			24	1.099
12	0	-11.2	28	0.095
			29	.375
			30	1.095
13	0	-35.8	31	0.103
			32	.383
			33	1.103

[a]All thermocouples were chromel-alumel.
[b]The accuracy of depth measurement is ±0.001 inch.

[redacted]

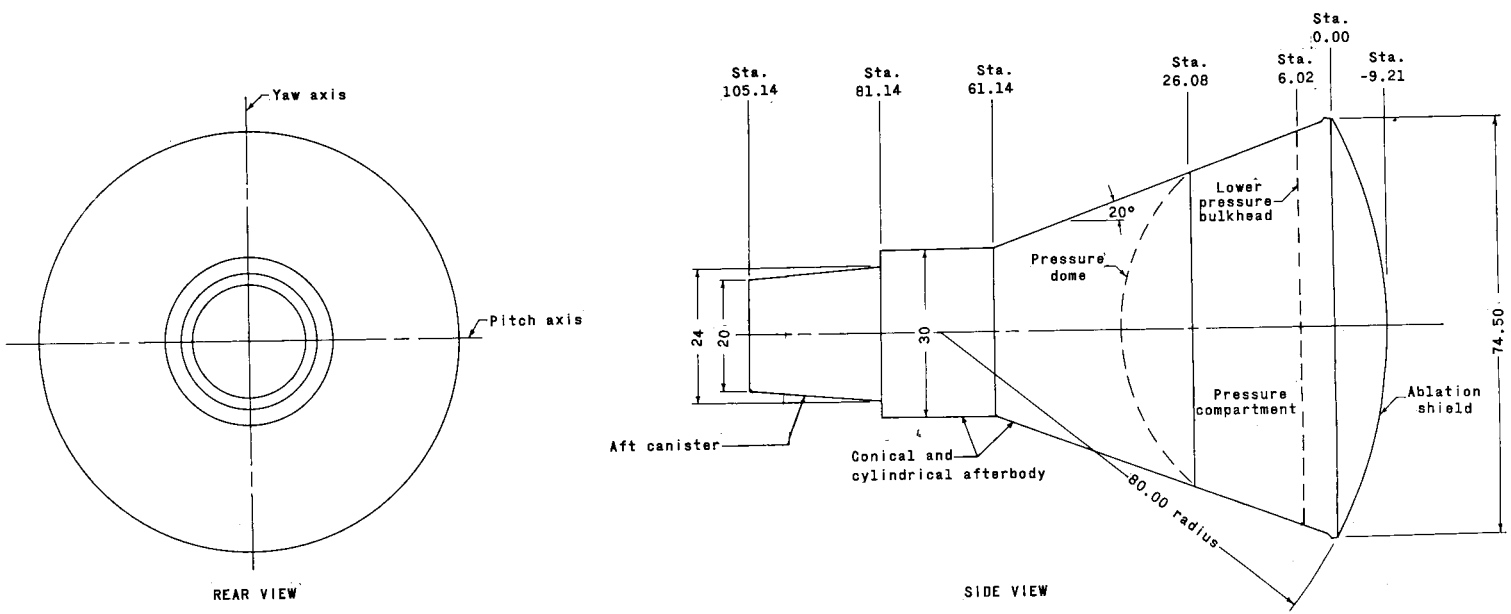

Figure 1.- Sketch of capsule. All dimensions are in inches.

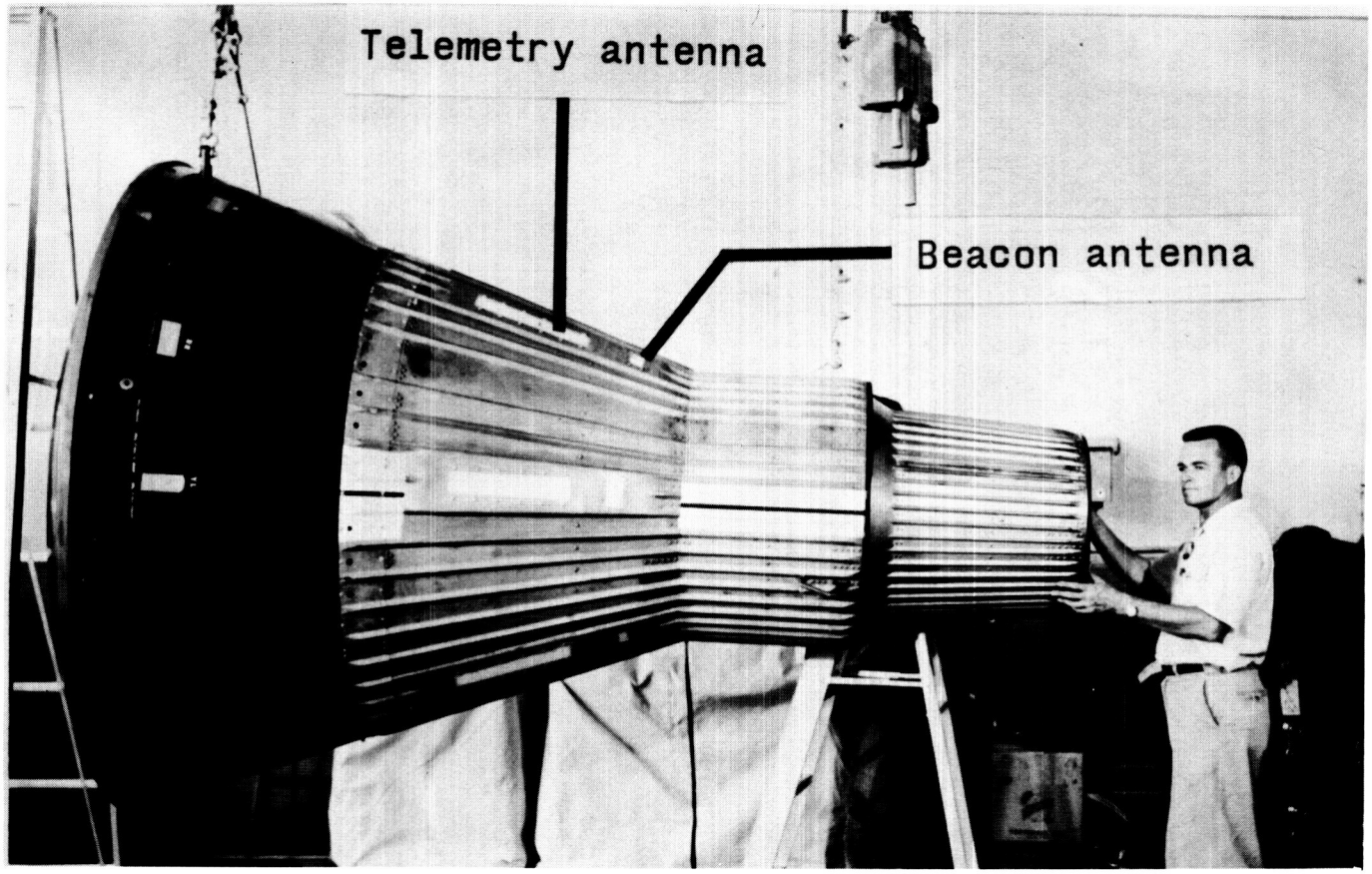

Figure 2.- Assembled capsule. G-60-2101

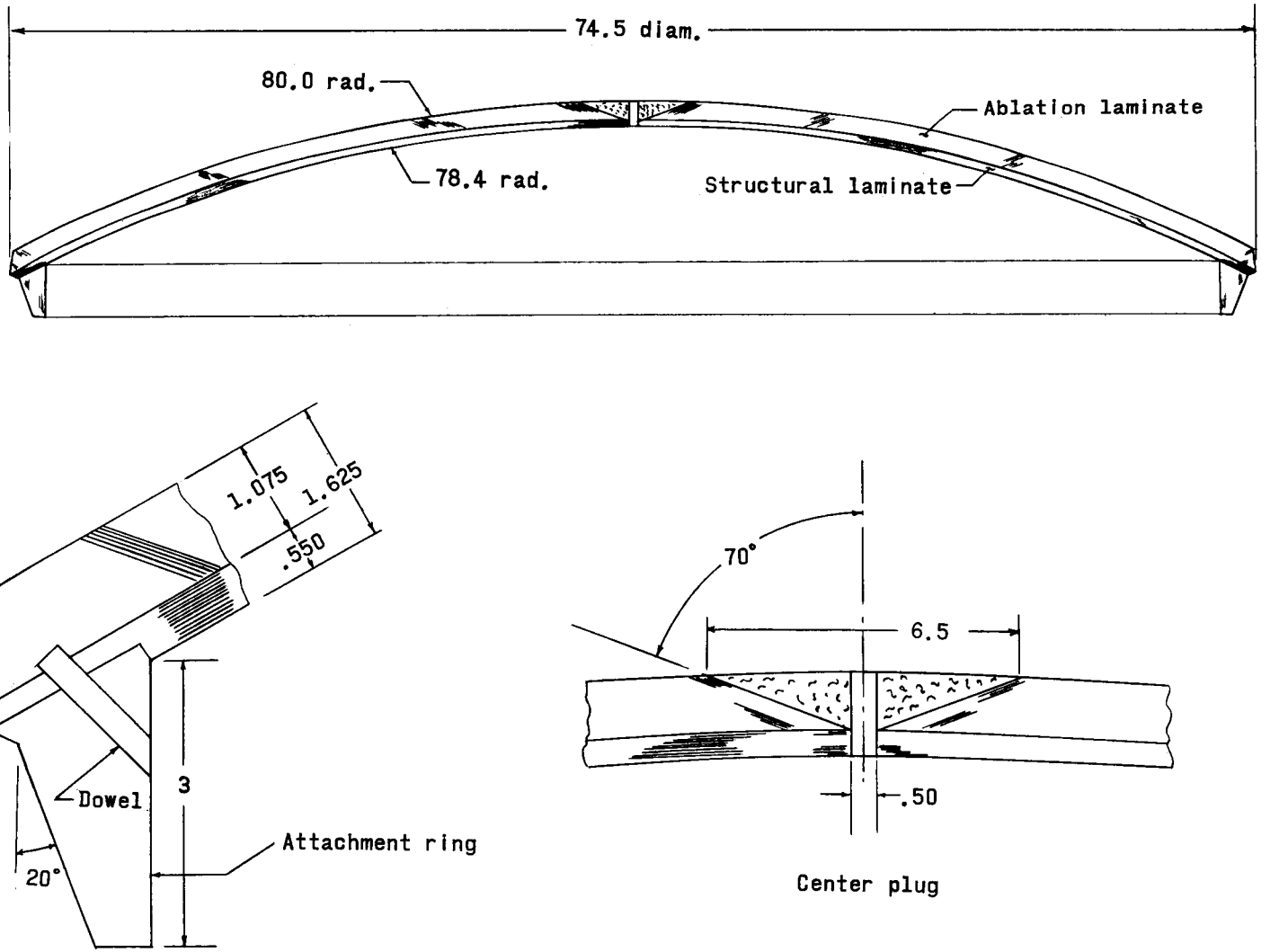

Figure 3.- Schematic drawing of heat shield. All dimensions are in inches unless otherwise noted.

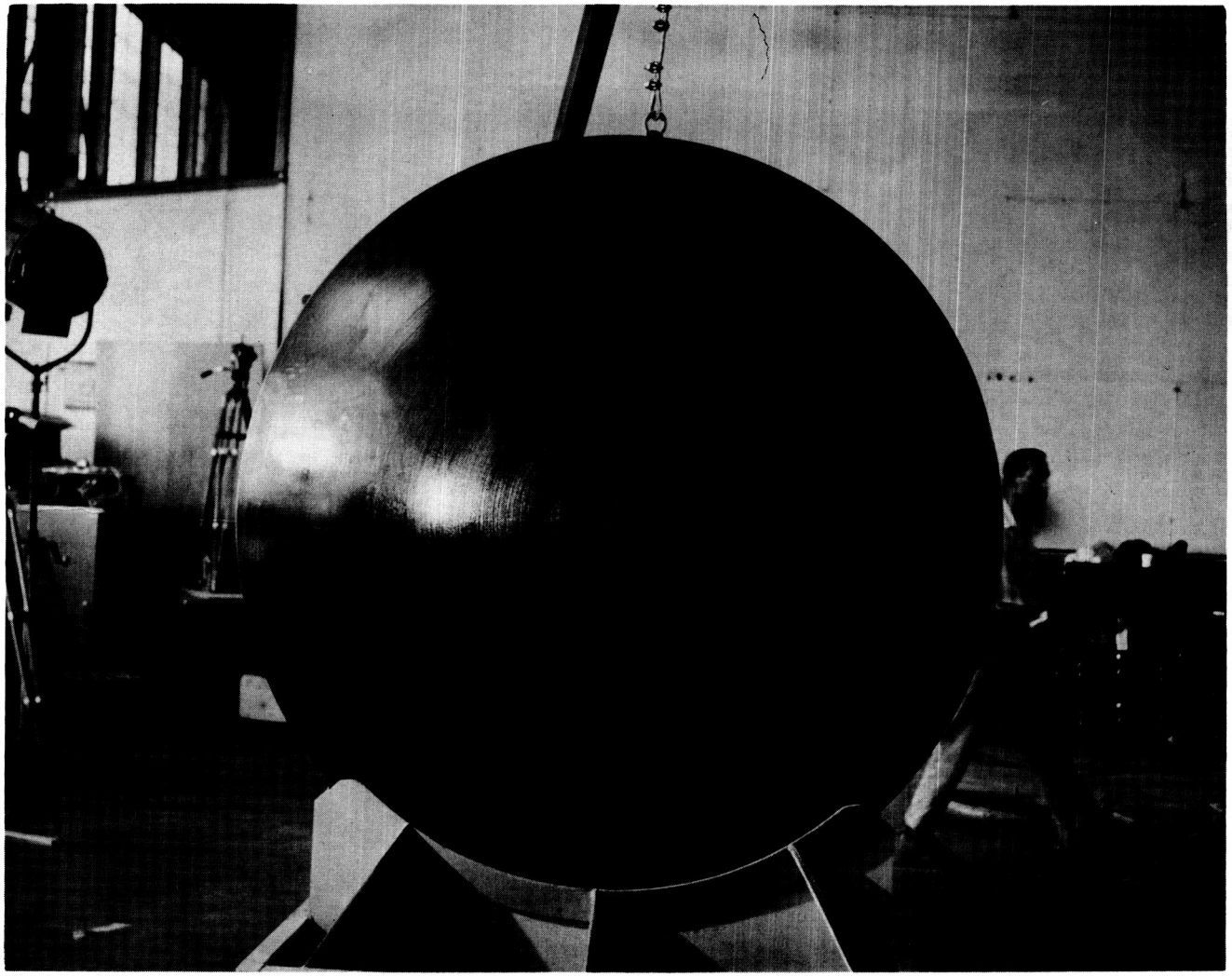

Figure 4.- Heat shield before test flight. G-60-2102

Figure 5.- Back view of heat shield, showing instrumentation leads. G-60-2103

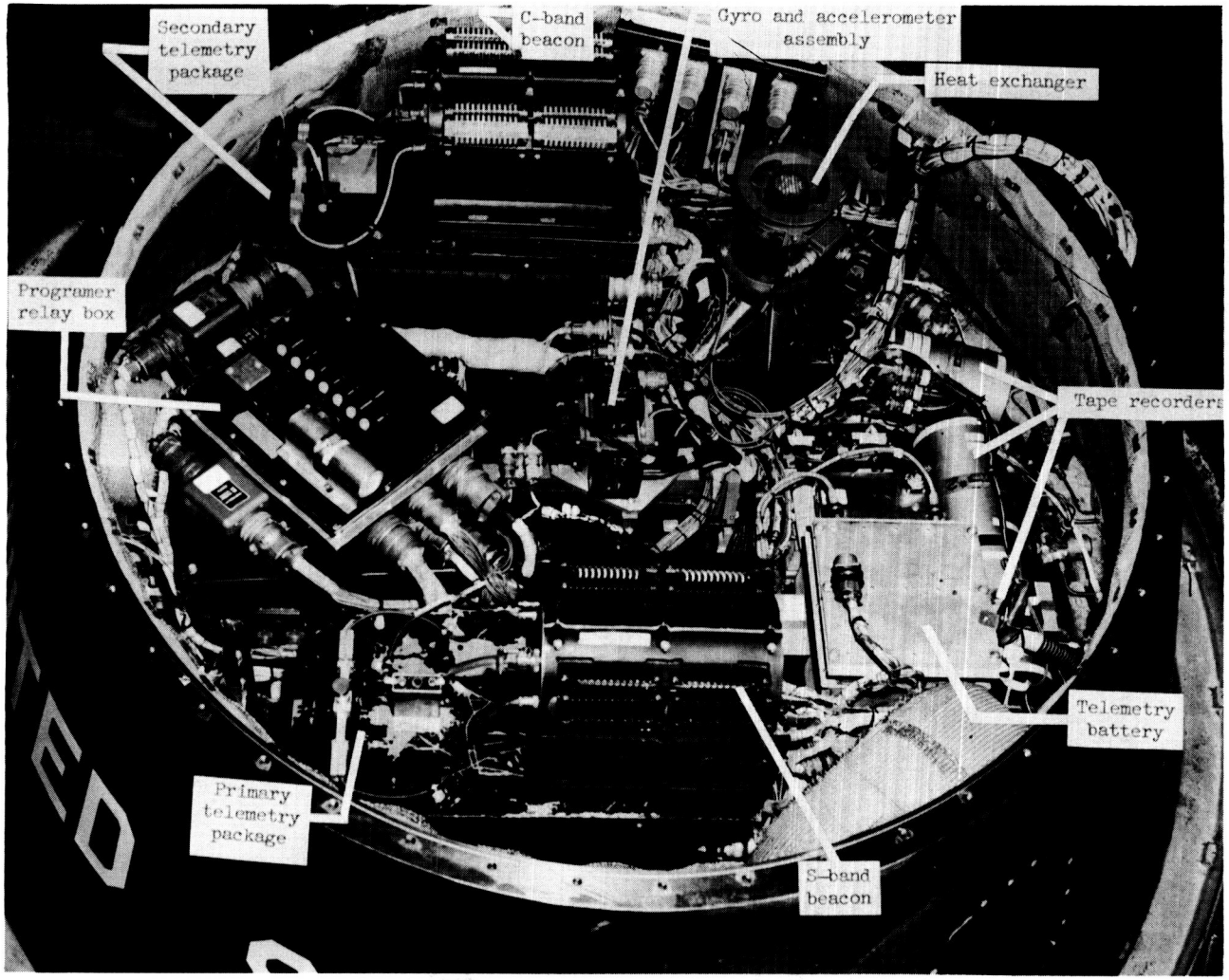

Figure 6.- Arrangement of instrumentation in pressurized compartment. G-60-2104

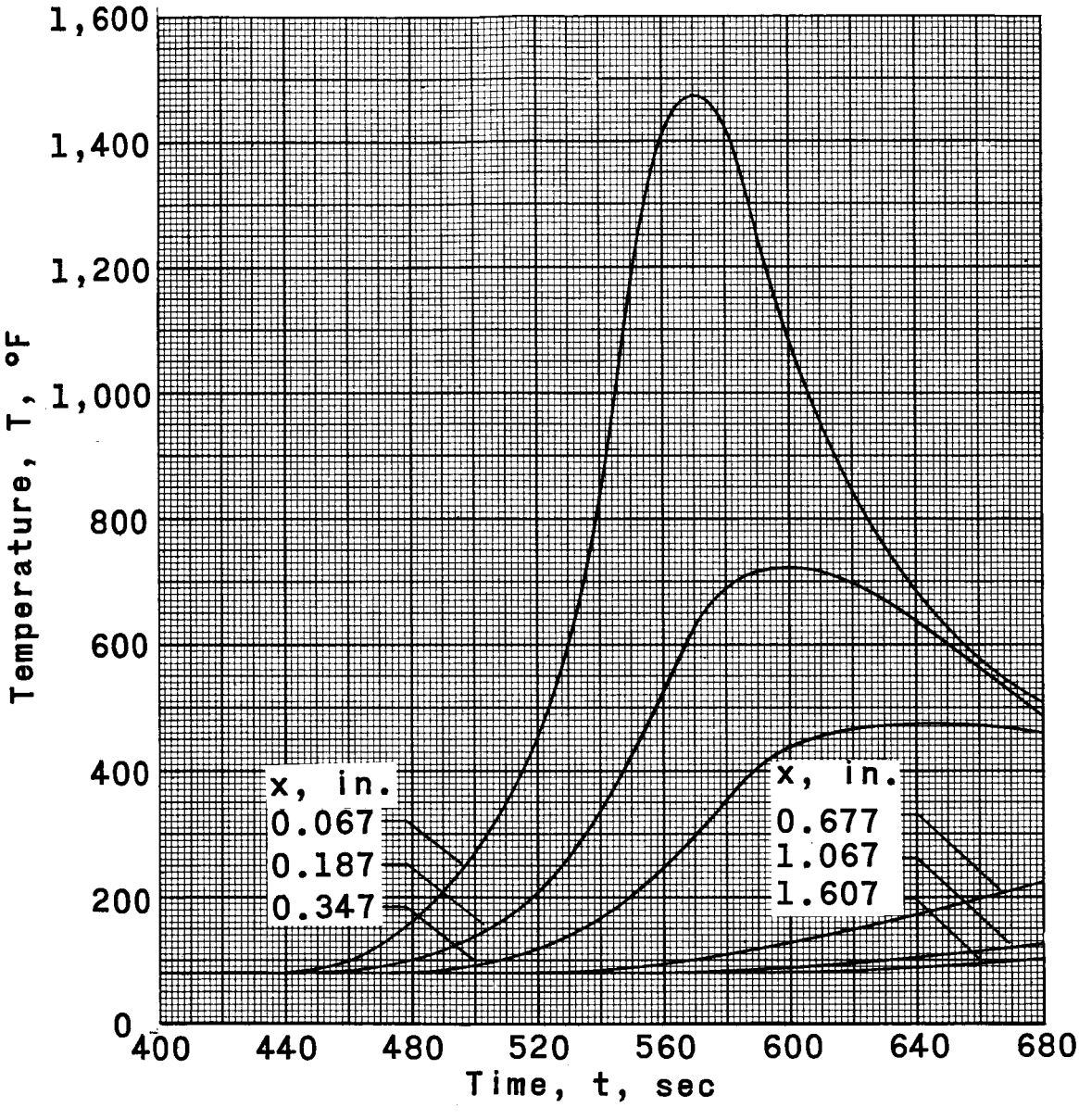

(a) Sensor 1.

Figure 7.- Measured heat-shield temperatures.

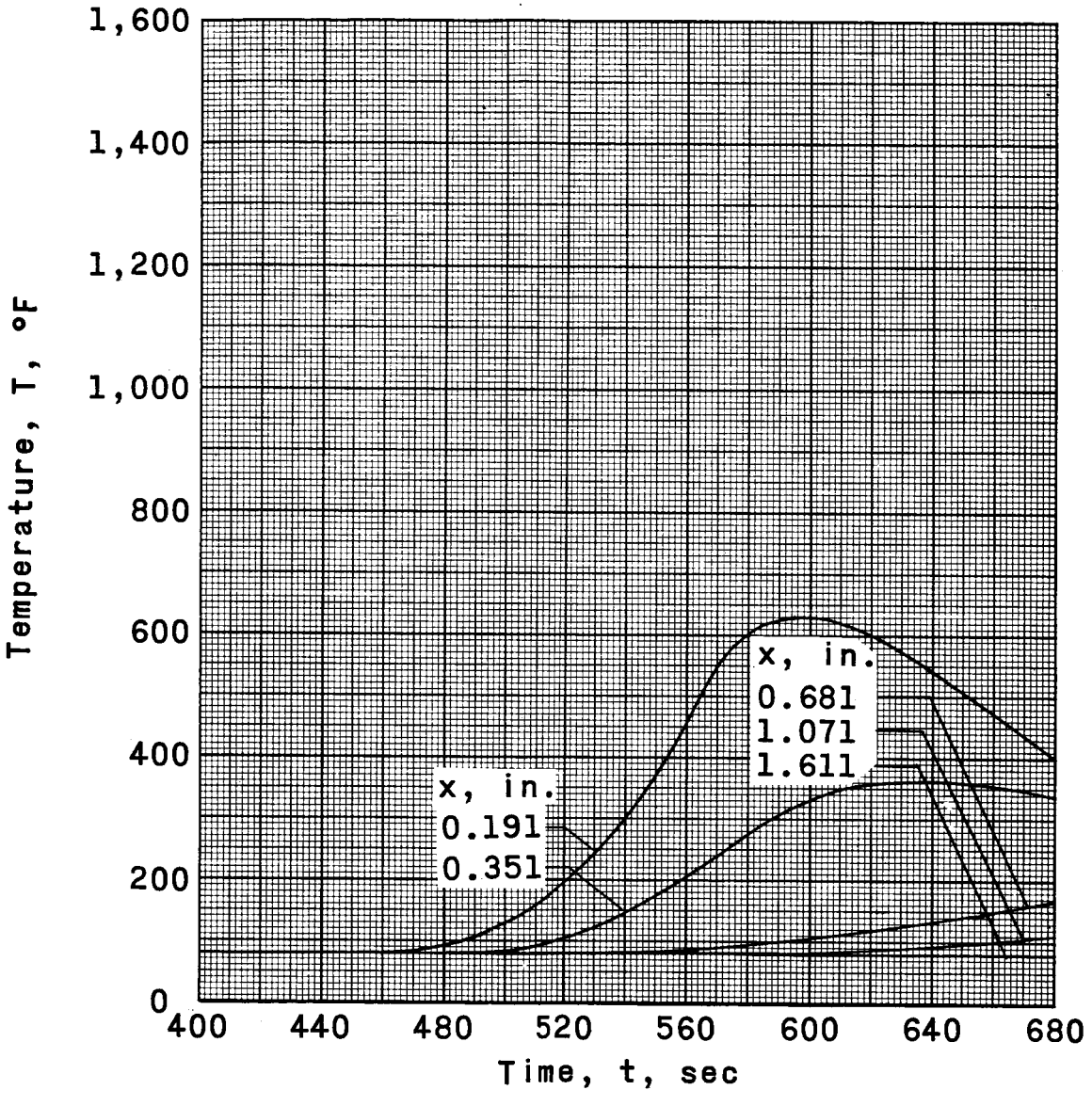

(b) Sensor 2.

Figure 7.- Continued.

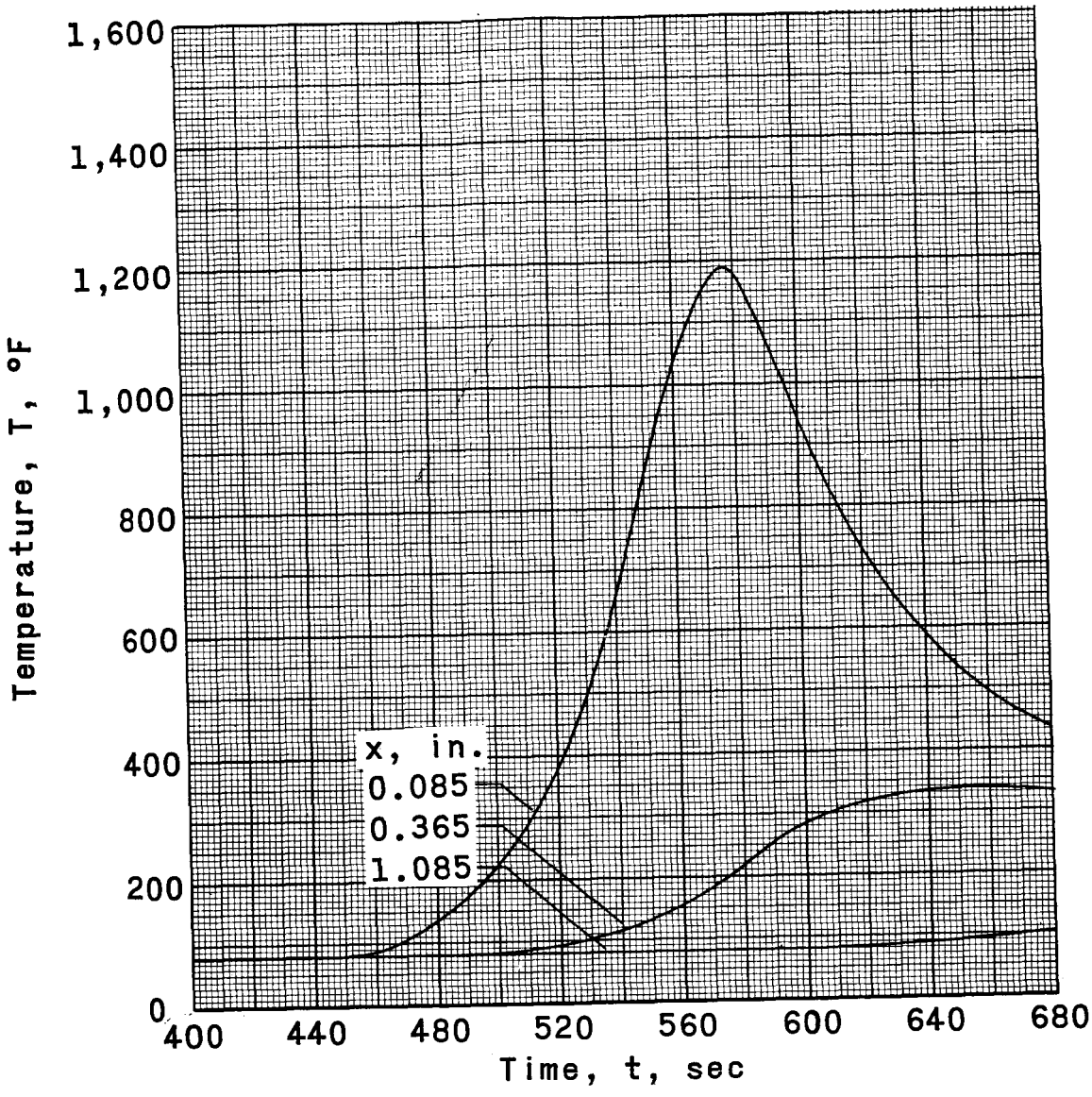

(c) Sensor 3.

Figure 7.- Continued.

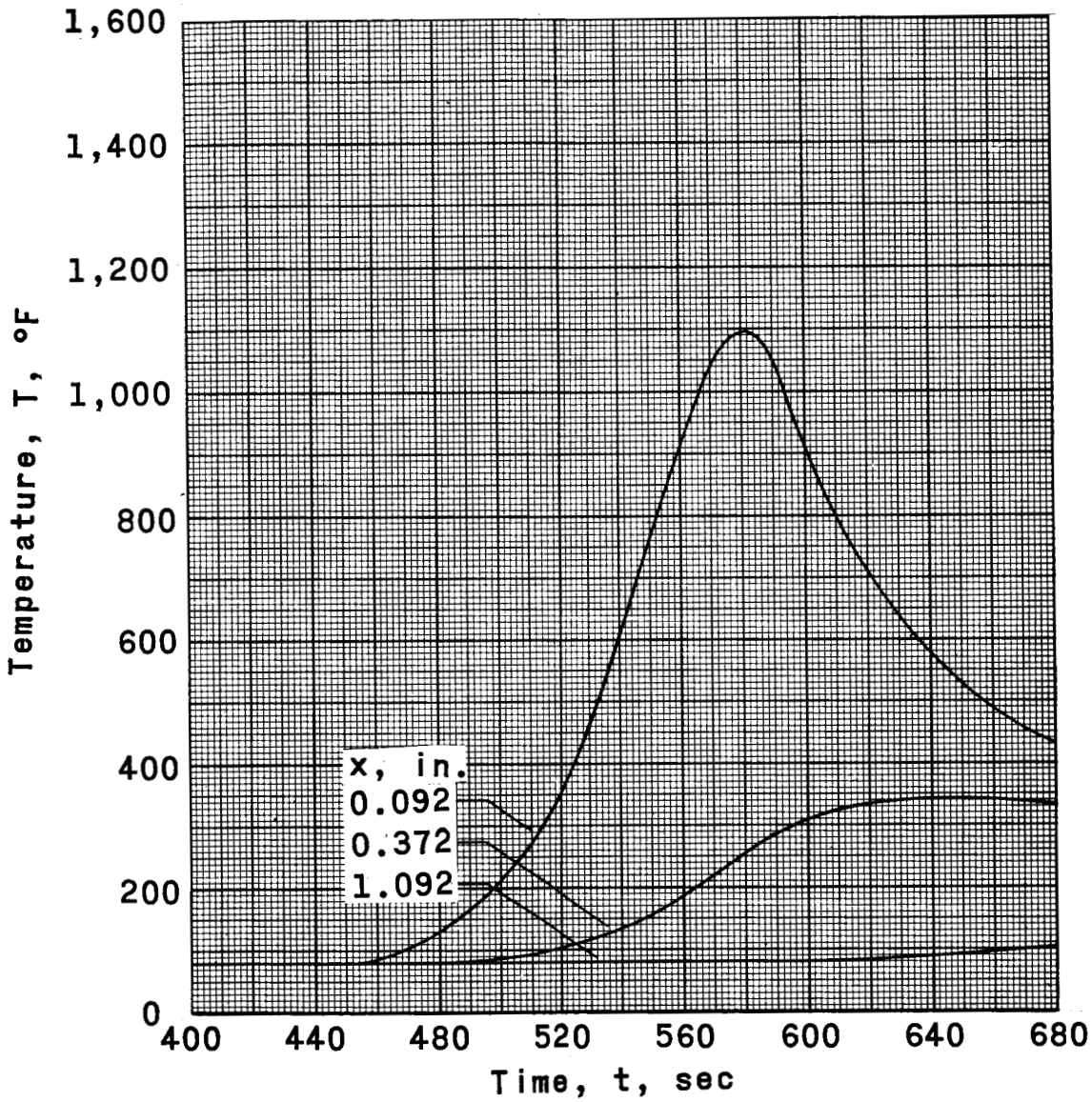

(d) Sensor 4.

Figure 7.- Continued.

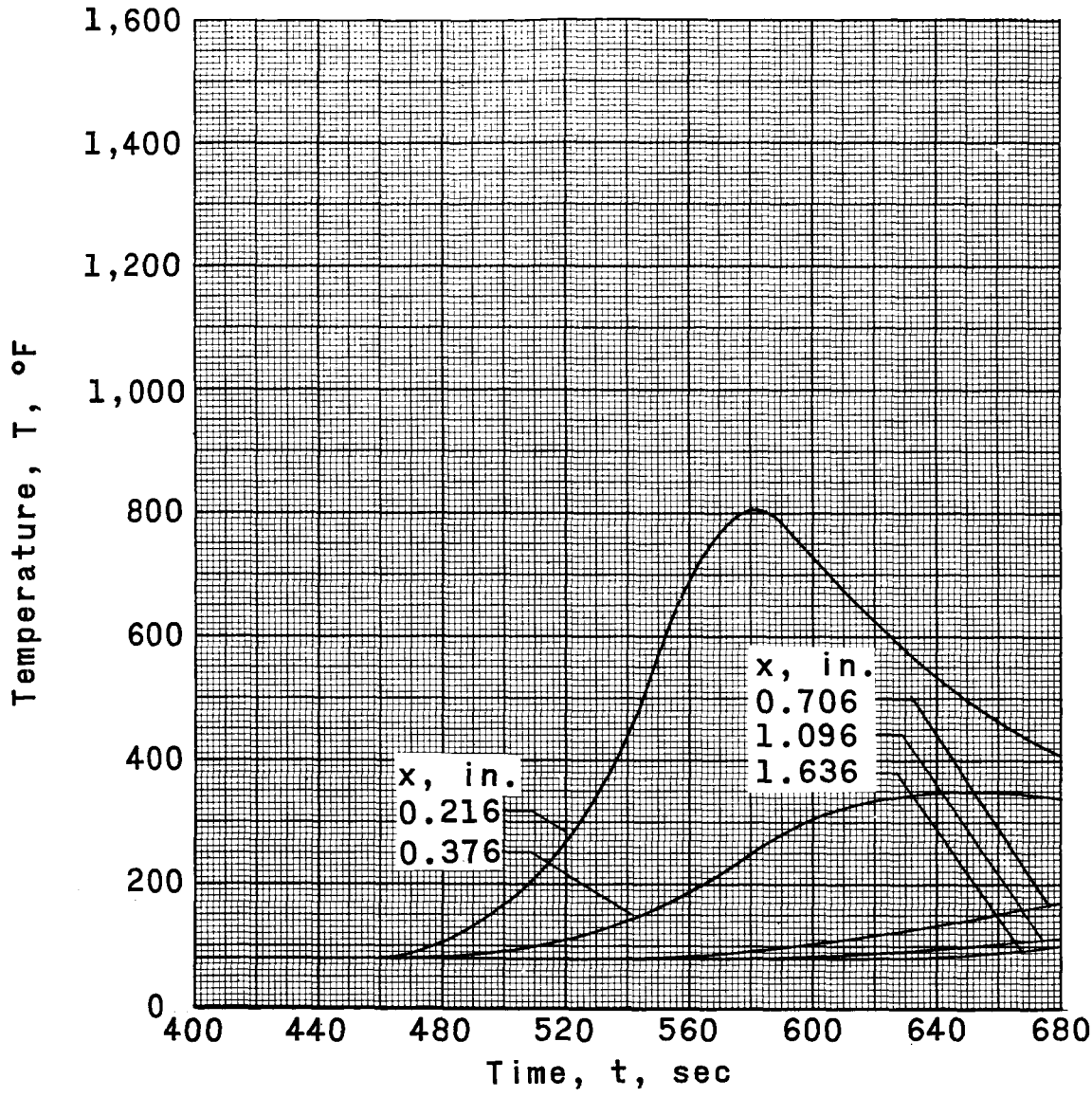

(e) Sensor 5.

Figure 7.- Continued.

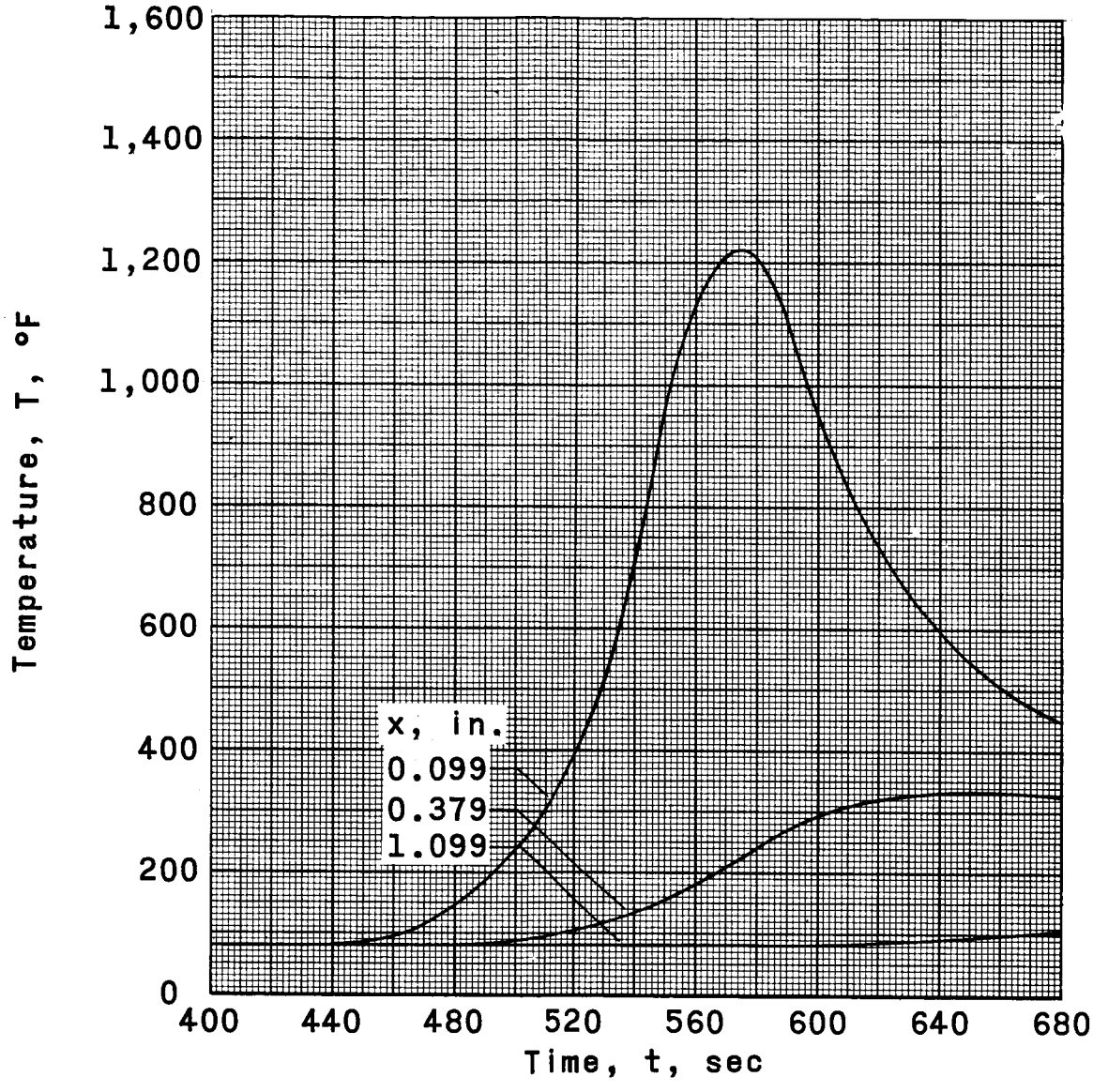

(f) Sensor 6.

Figure 7.- Continued.

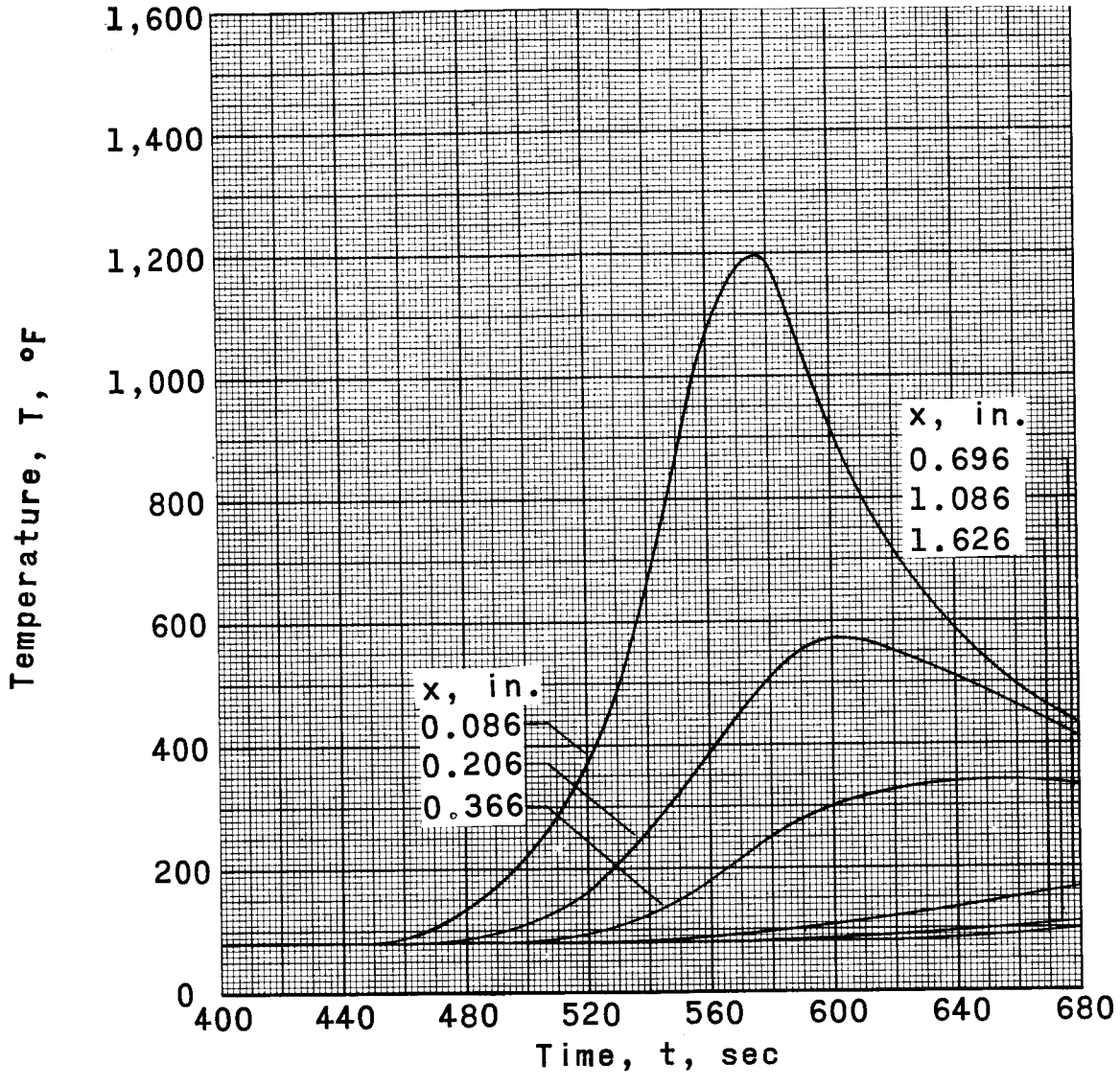

(g) Sensor 7.

Figure 7.- Continued.

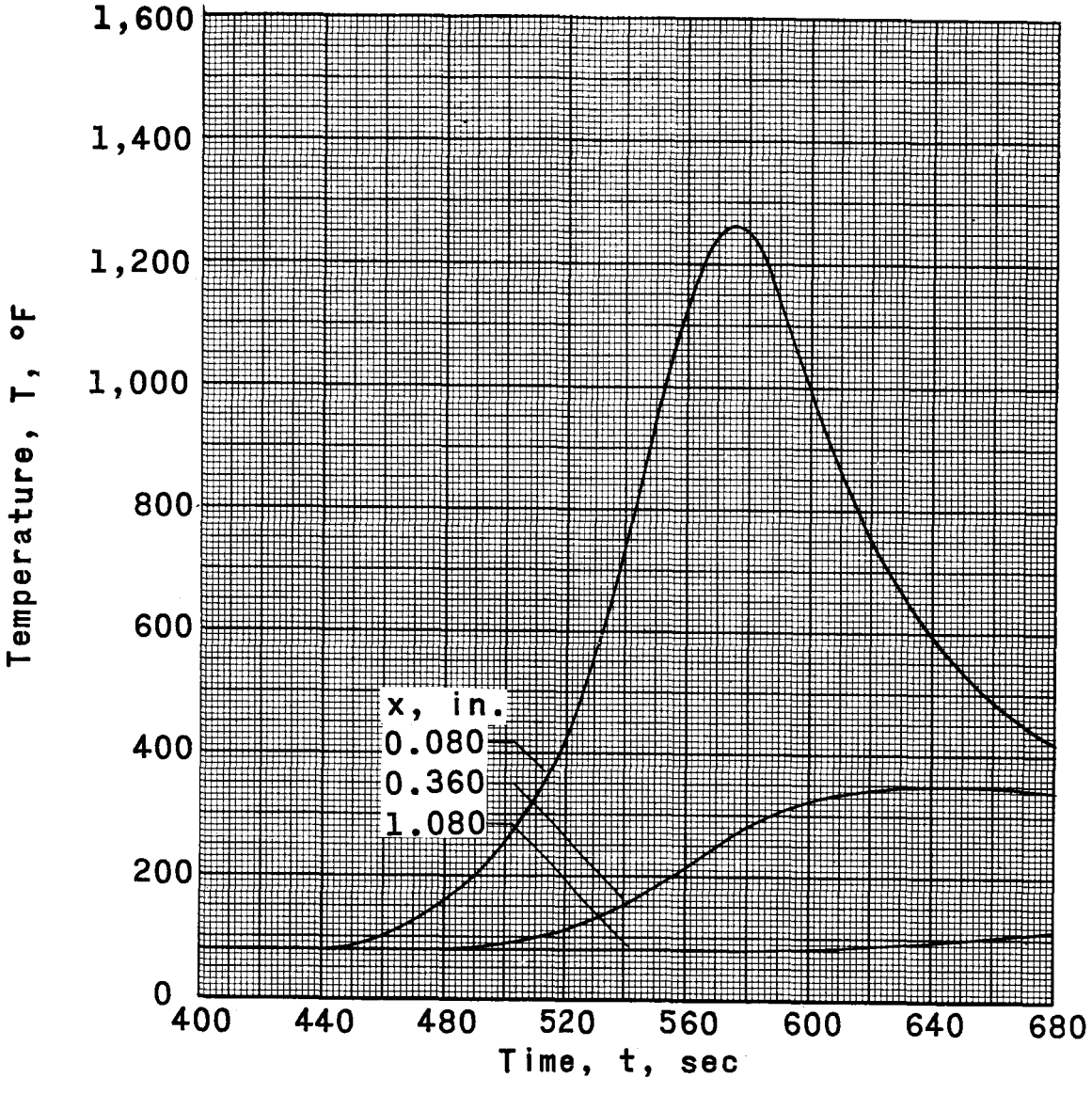

(h) Sensor 8.

Figure 7.- Continued.

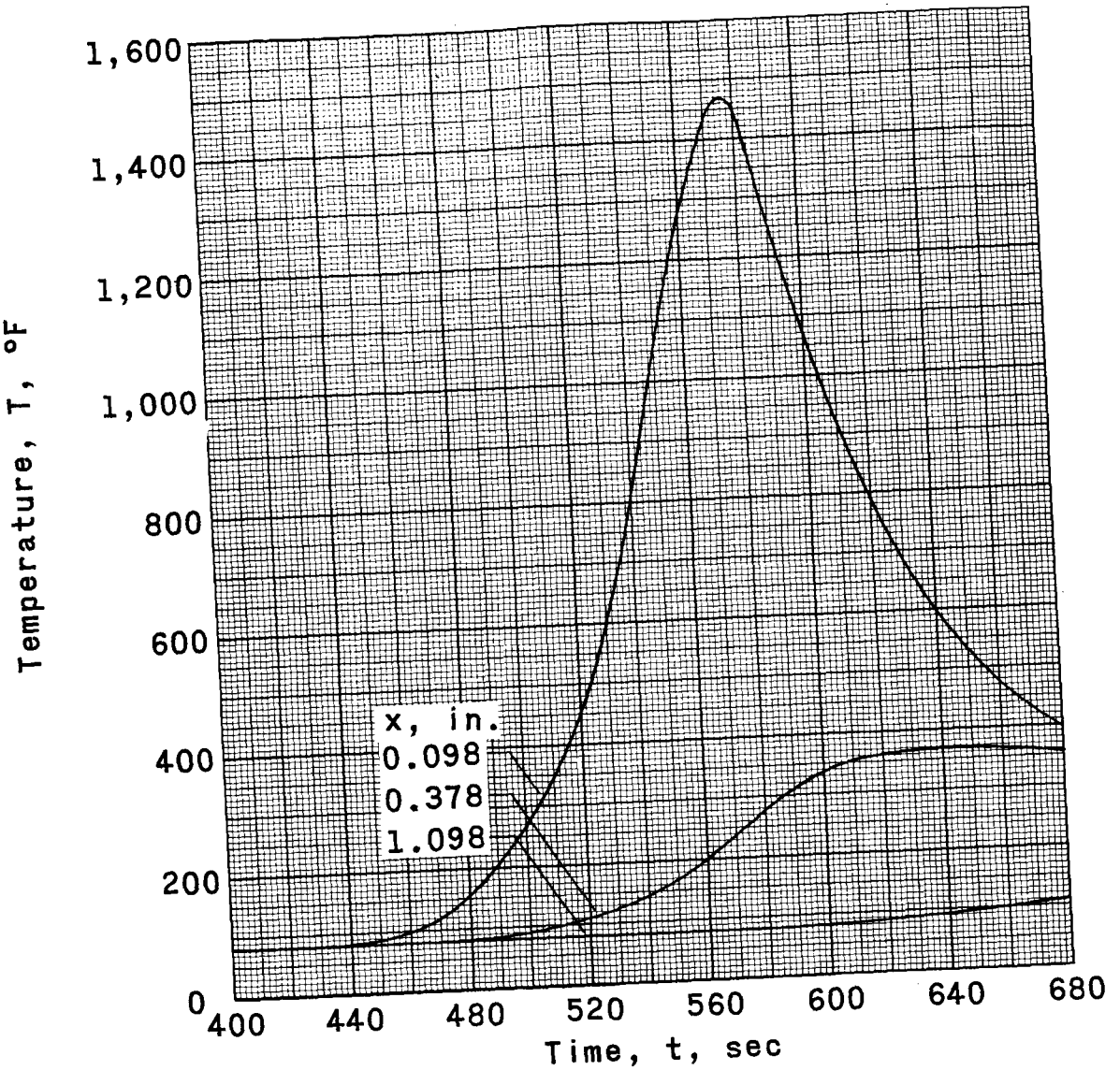

(i) Sensor 9.

Figure 7.- Continued.

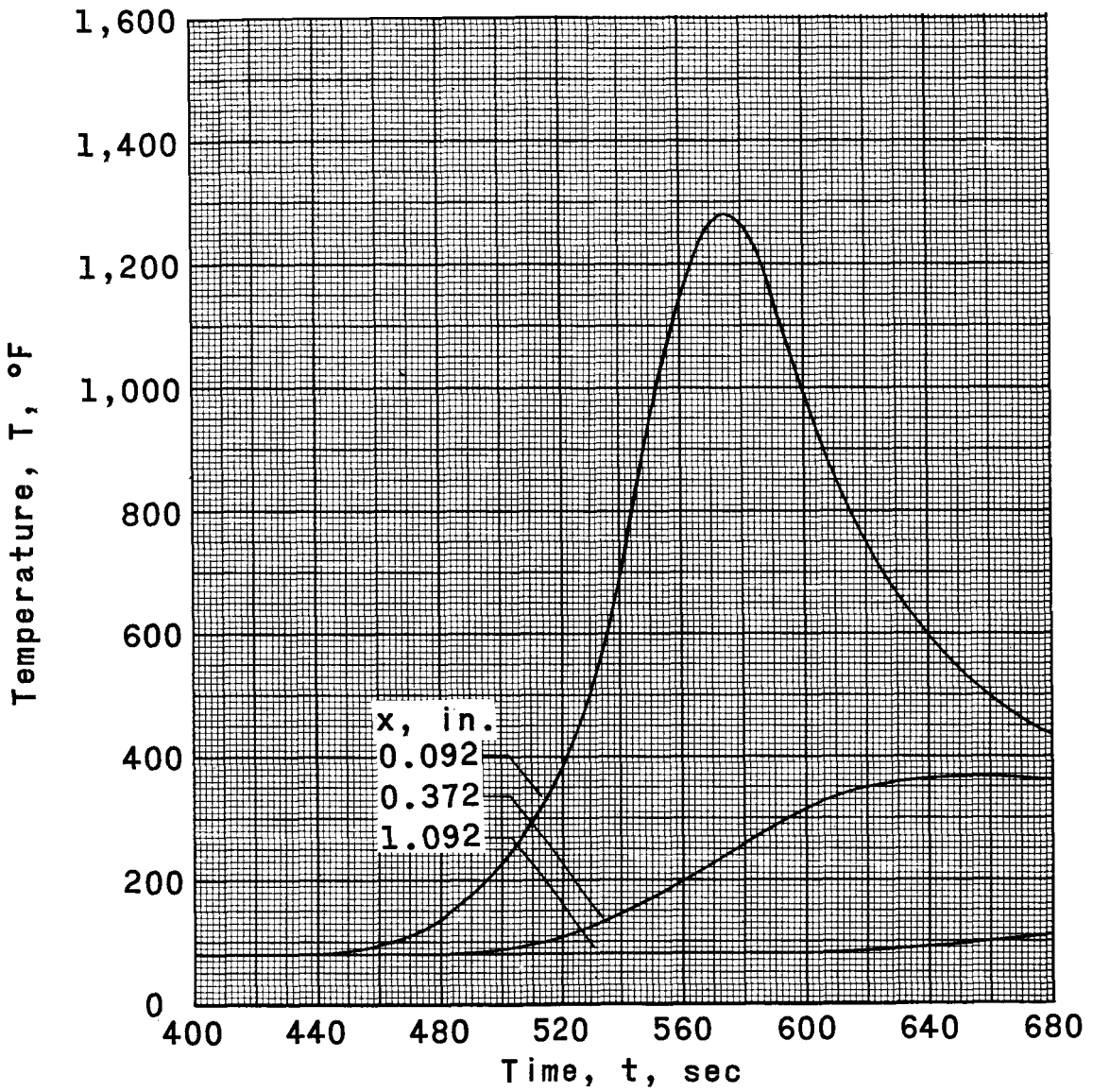

(j) Sensor 10.

Figure 7.- Continued.

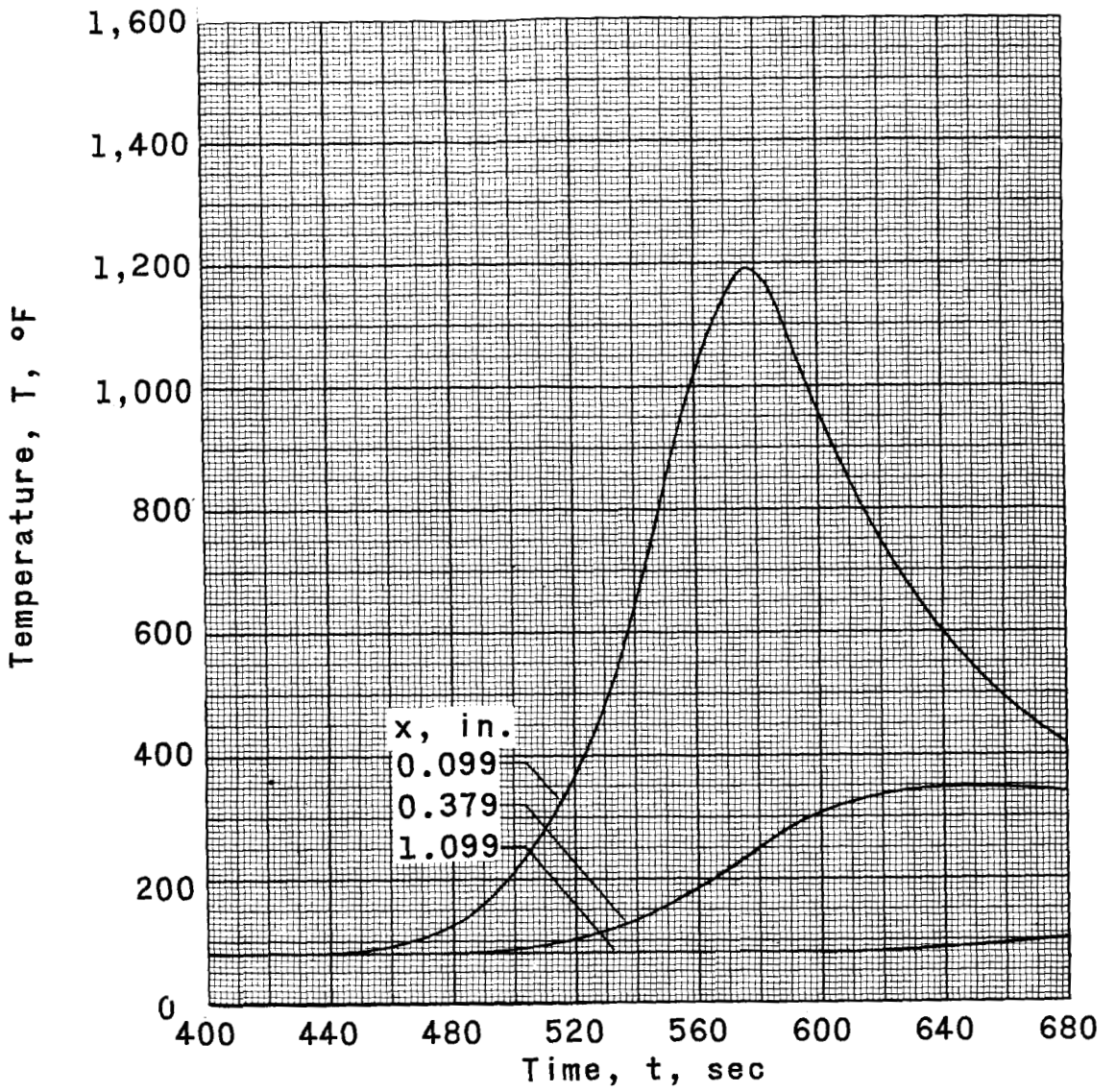

(k) Sensor 11.

Figure 7.- Continued.

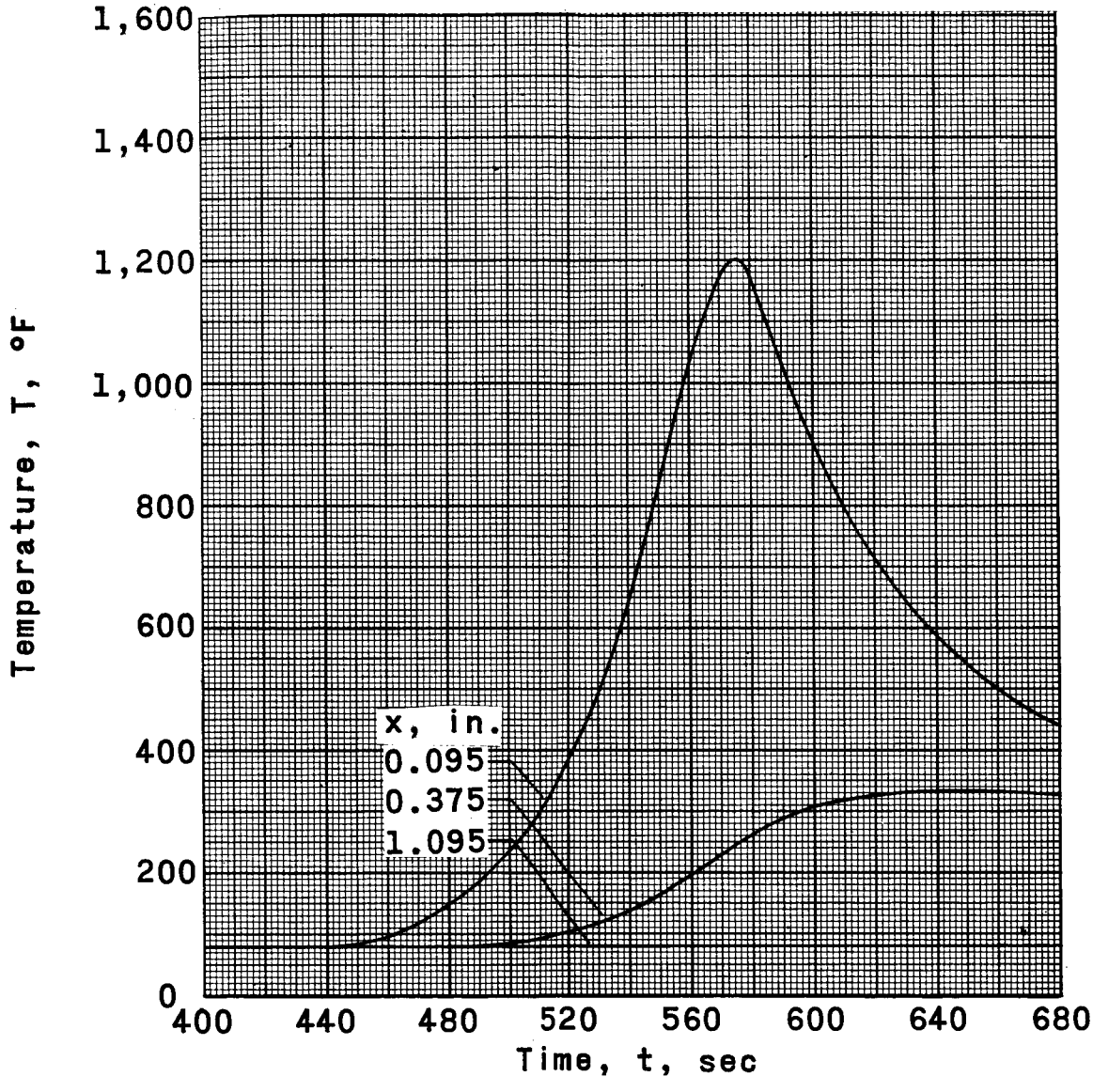

(*l*) Sensor 12.

Figure 7.- Continued.

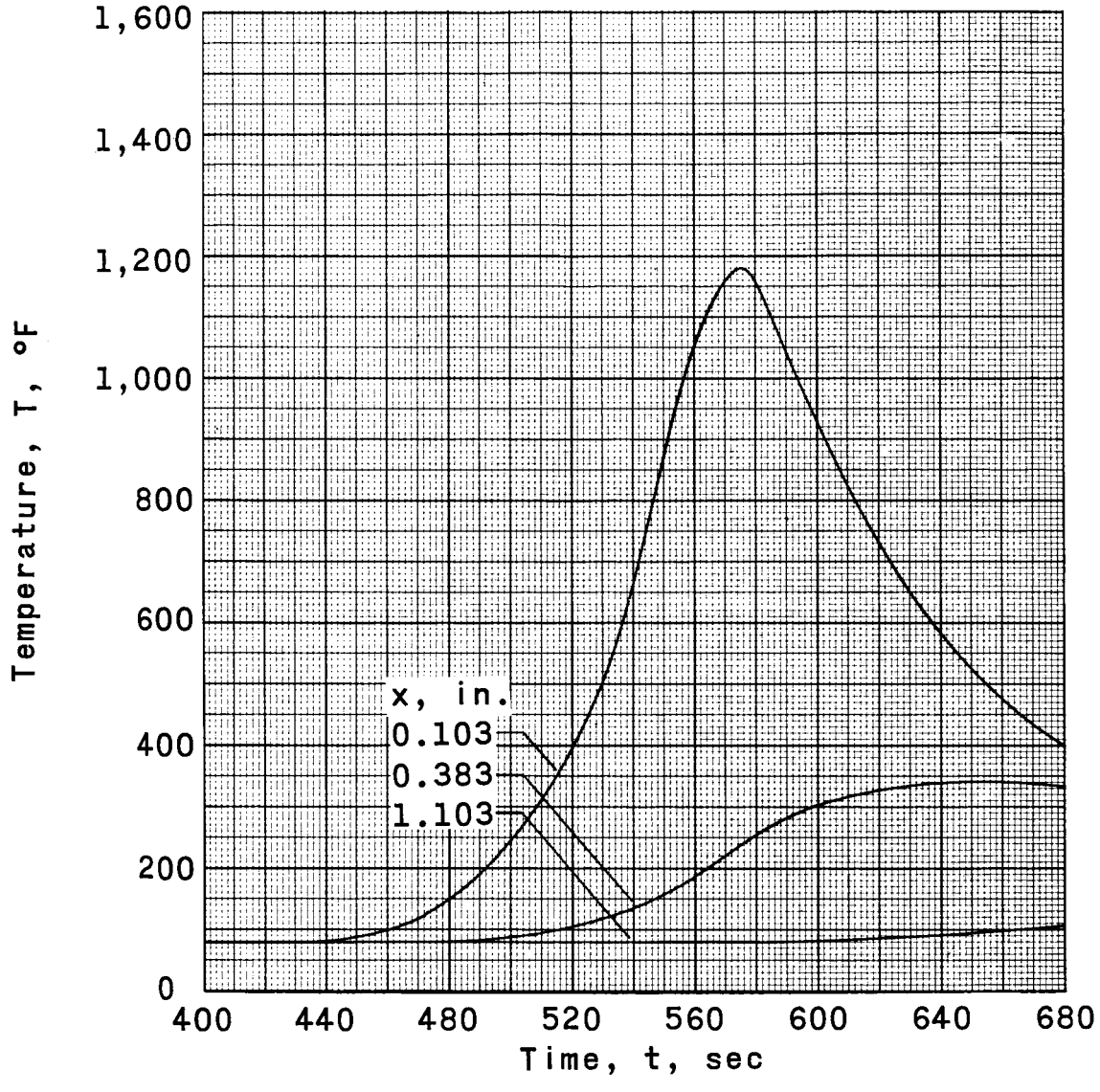

(m) Sensor 13.

Figure 7.- Concluded.

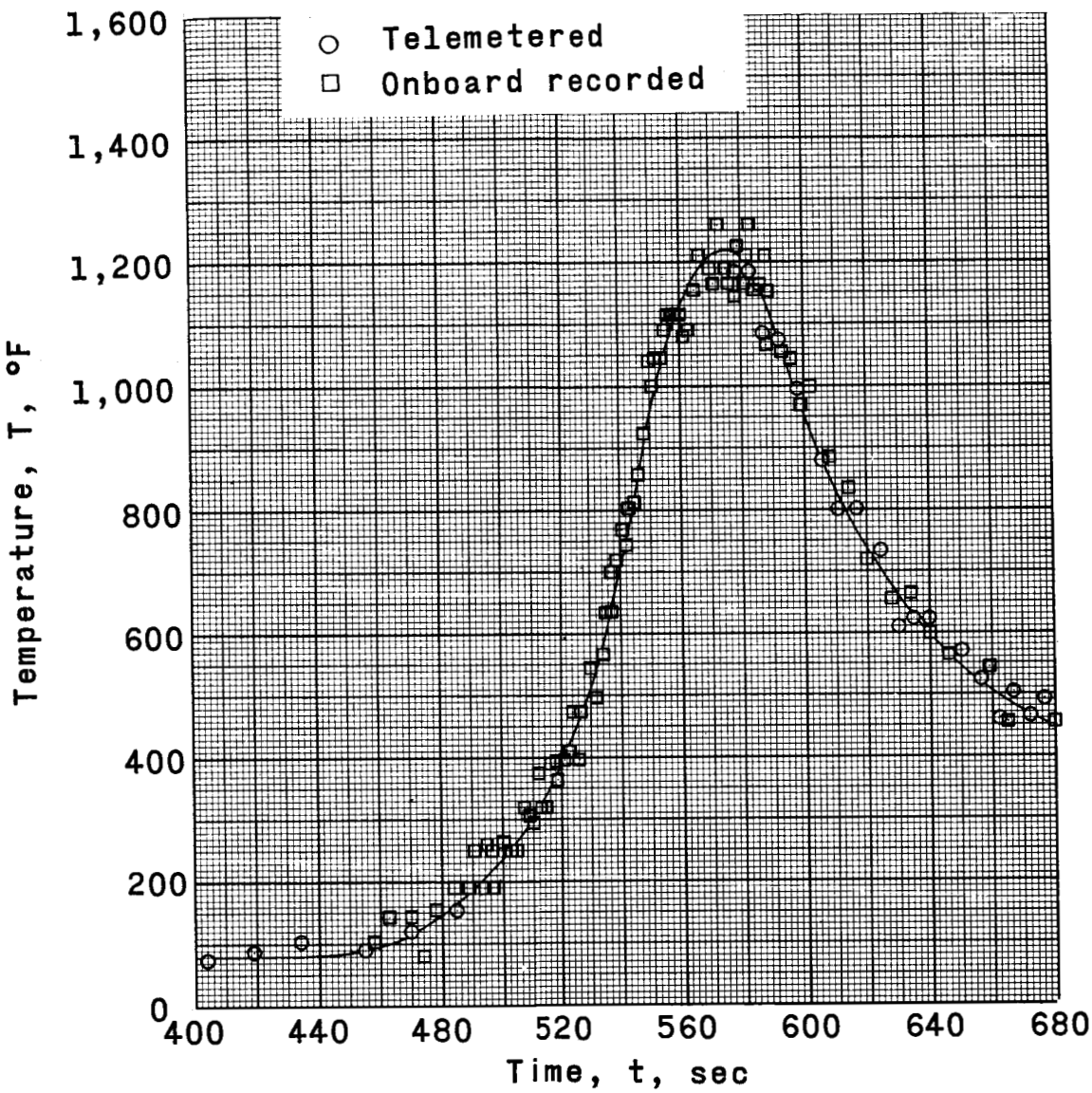

Figure 8.- Typical thermocouple data.
(Thermocouple 10.)

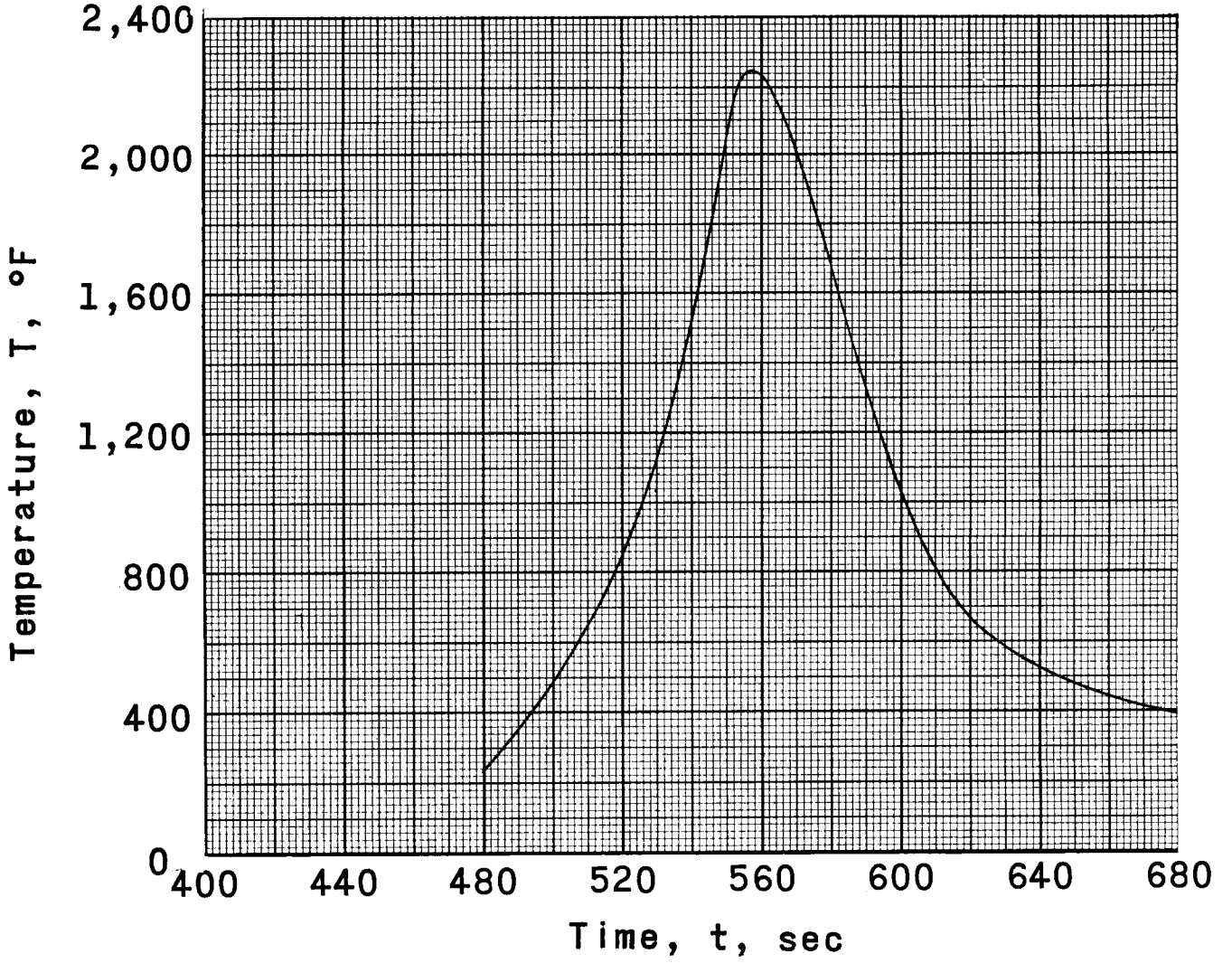

Figure 9.- Calculated surface temperature of heat shield.

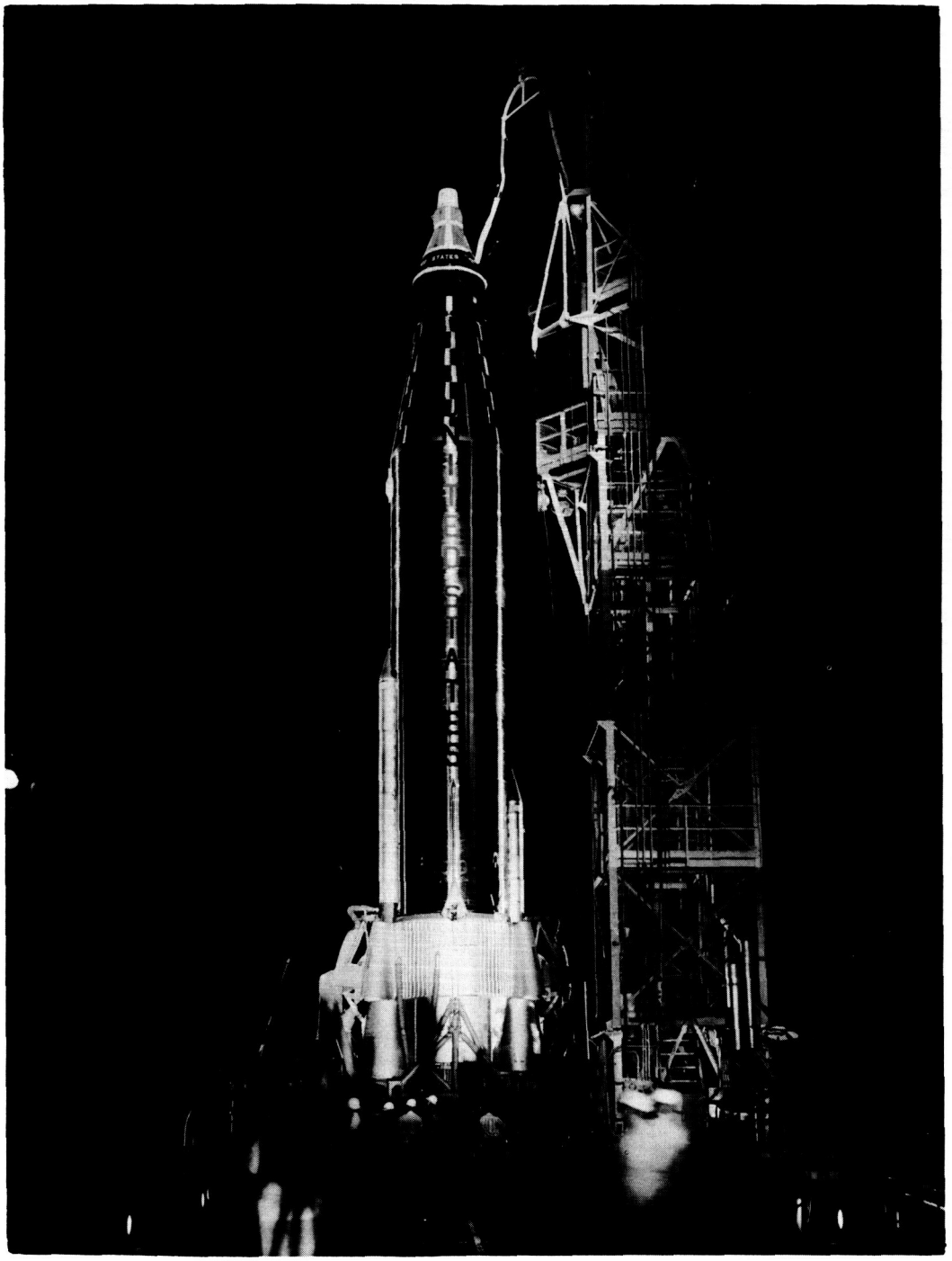

G-60-2105

Figure 10.- Capsule mounted on Atlas 10D booster on launch stand.

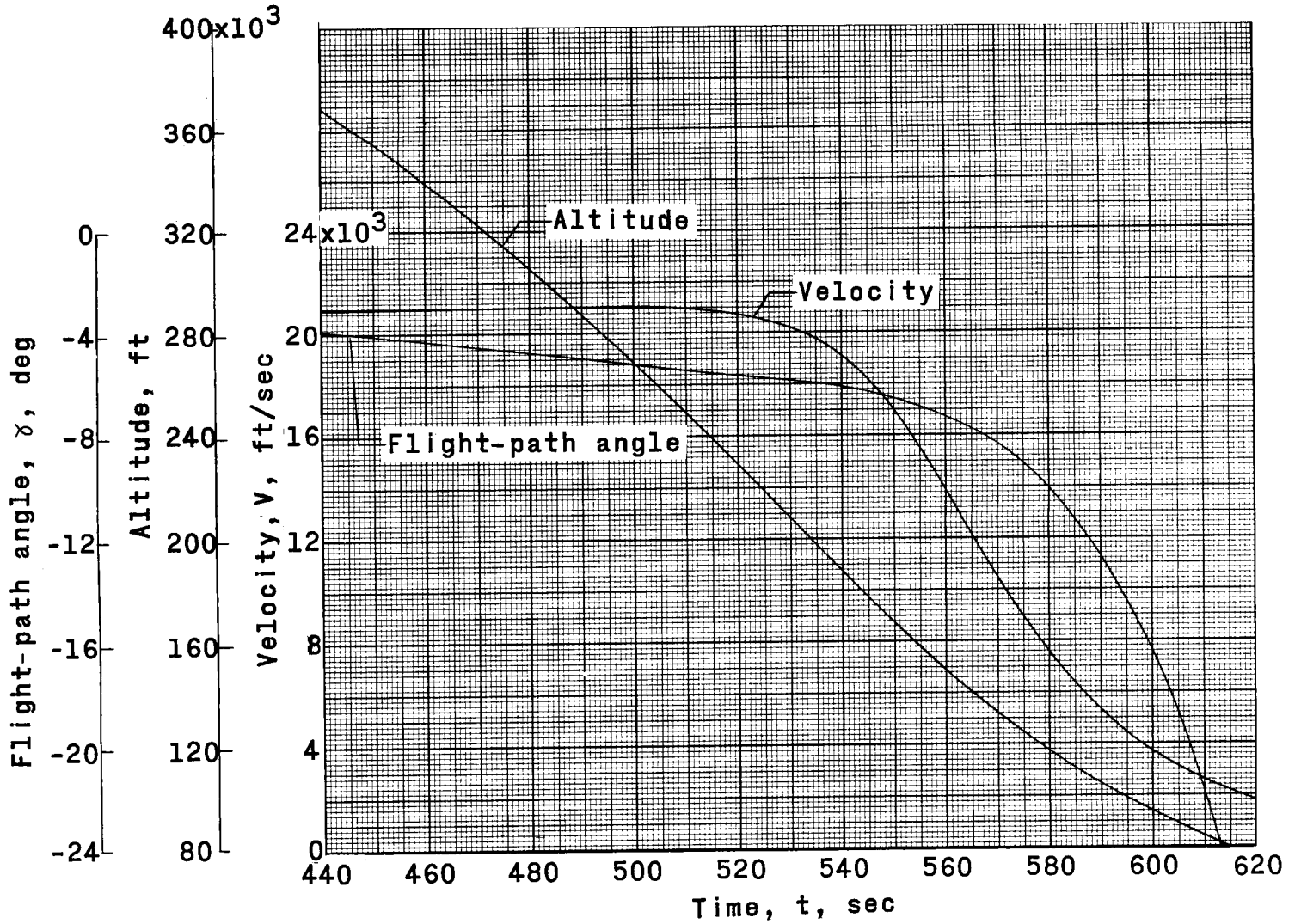

Figure 11.- Atmospheric-entry trajectory.

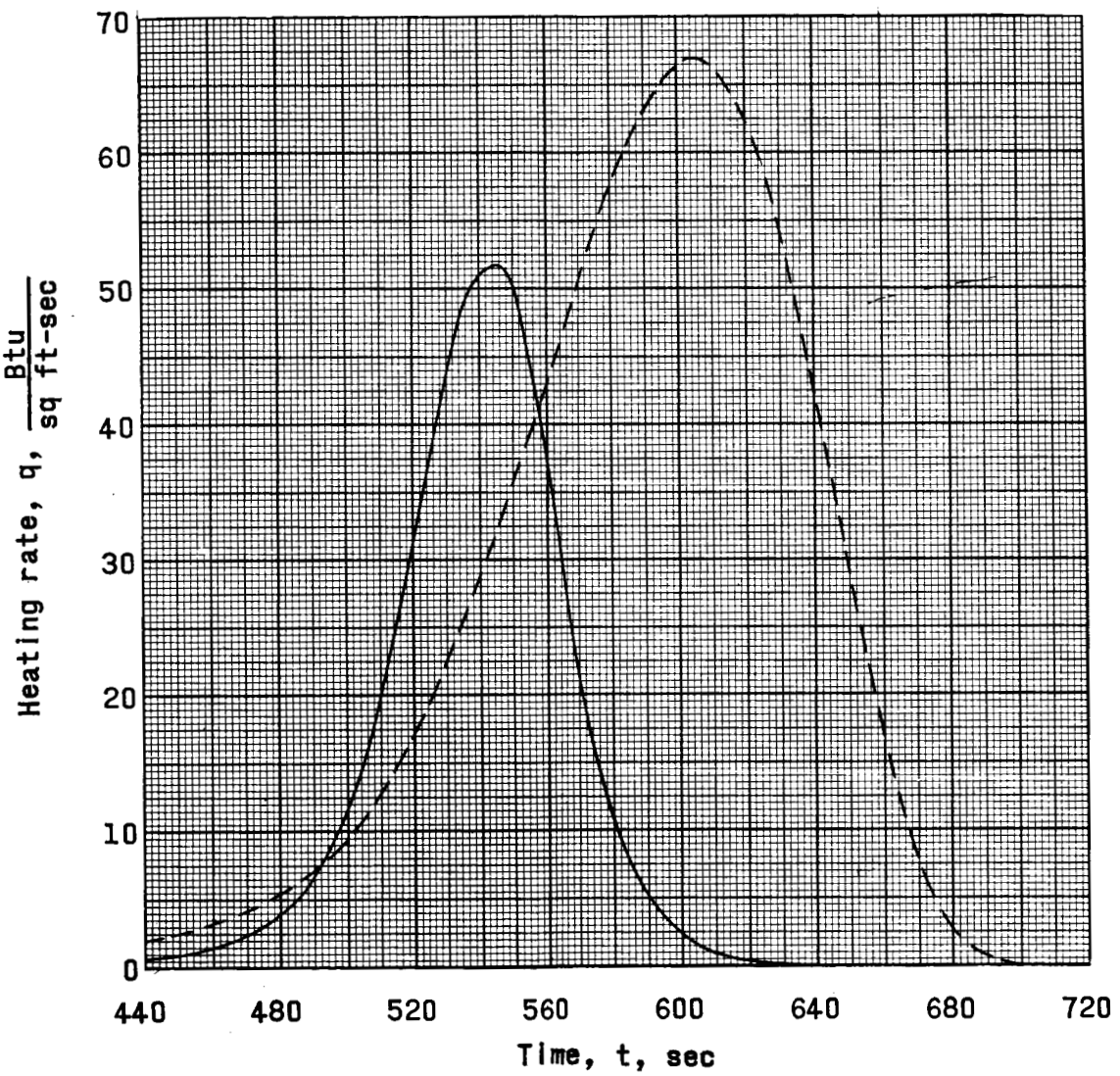

Figure 12.- Comparison of stagnation-point heating rates for achieved and anticipated flight trajectories. $H_S = 0$.

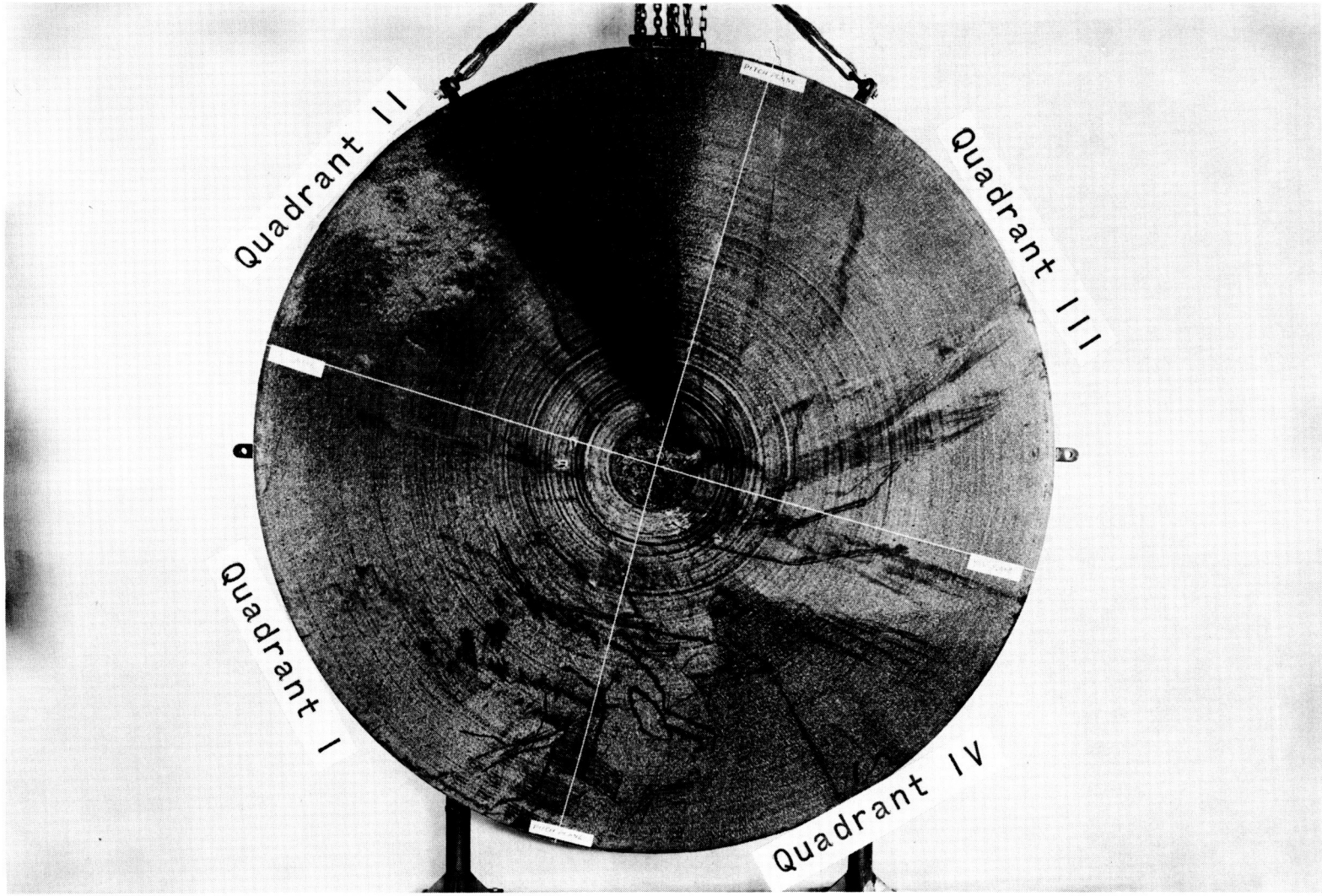

Figure 13.- Recovered heat shield. G-60-2106

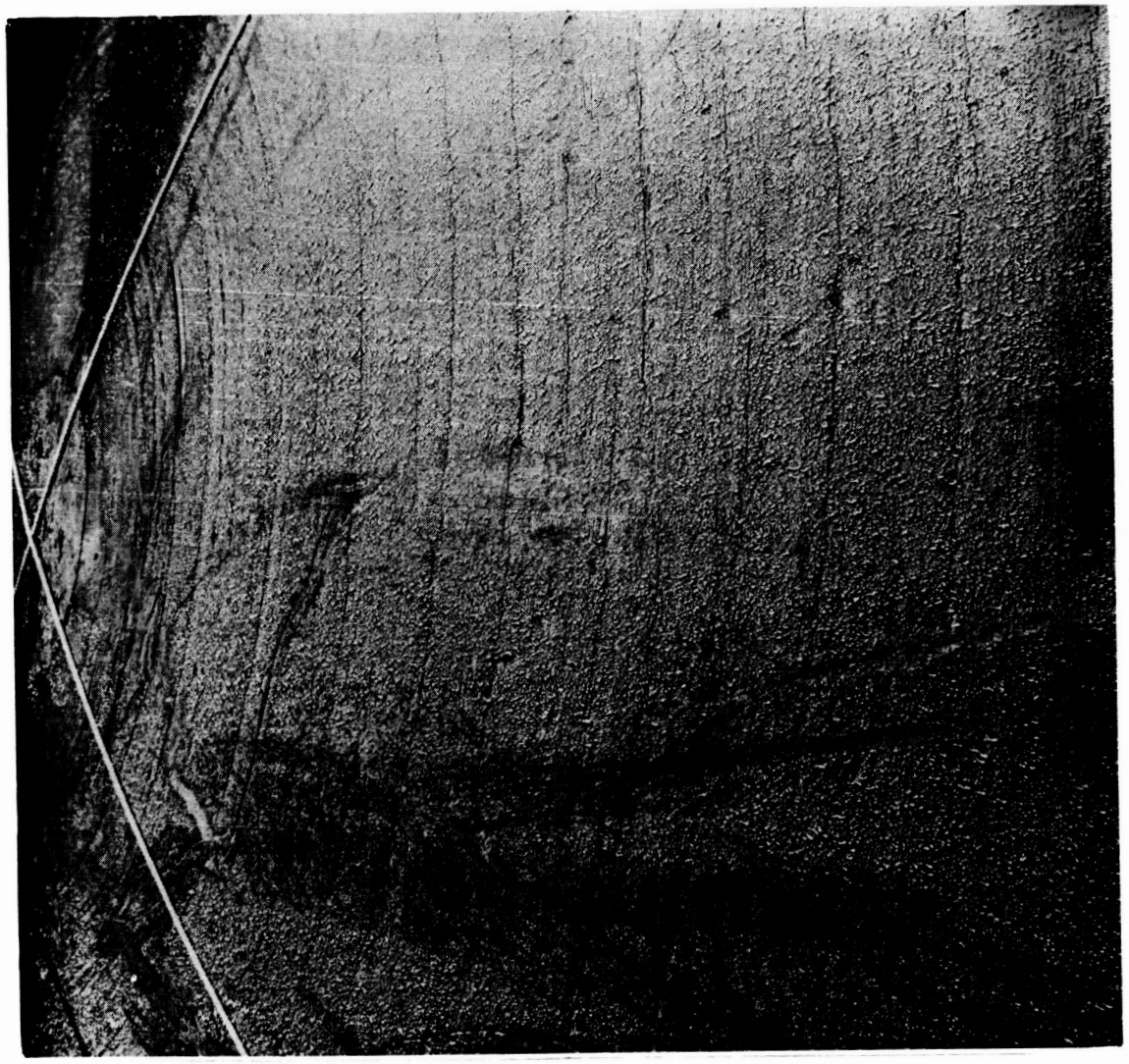

B-59-504

Figure 14.- Closeup photograph of surface of recovered heat shield.

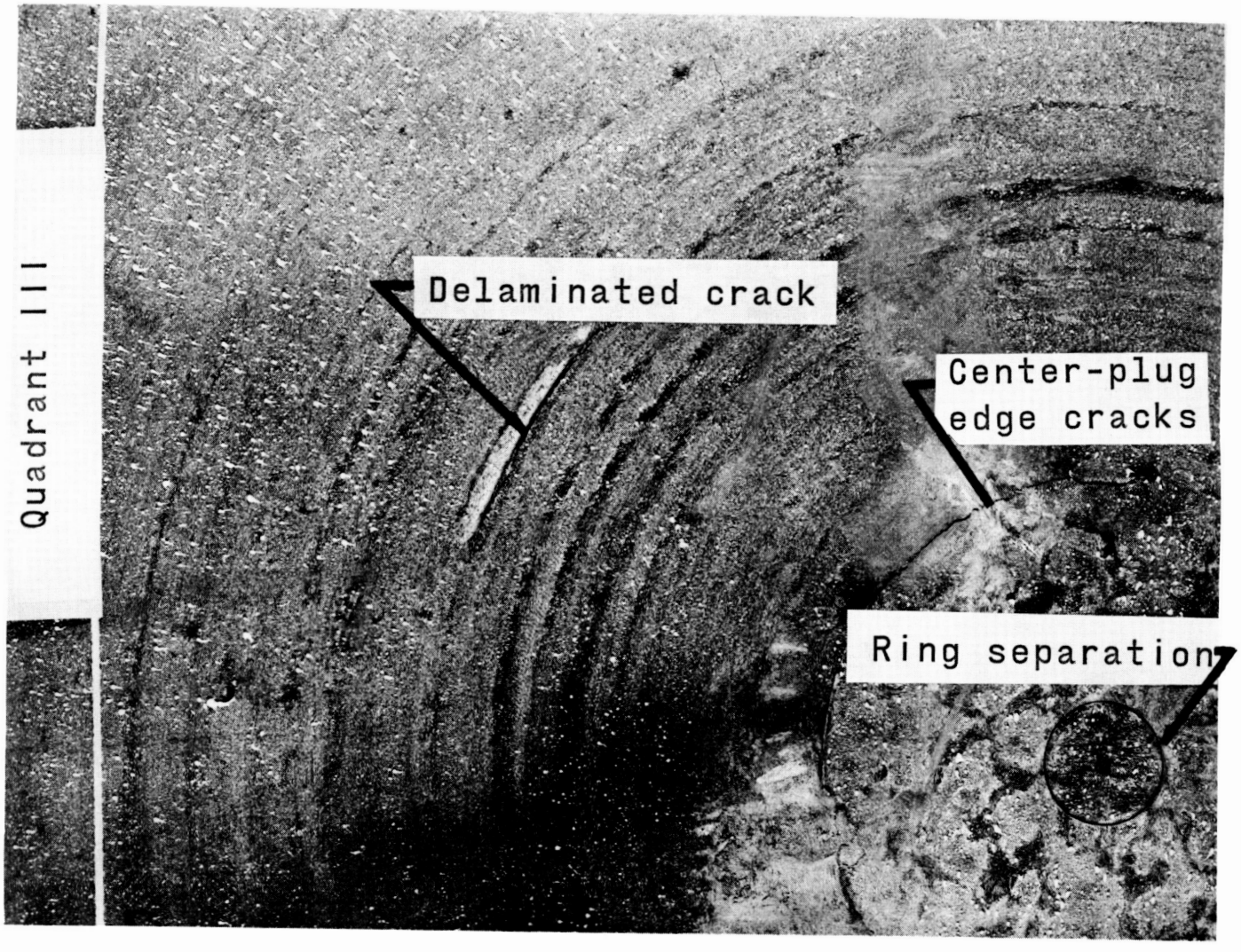

G-60-2107

Figure 15.- Photograph of heat shield showing effects of atmospheric-entry heating.

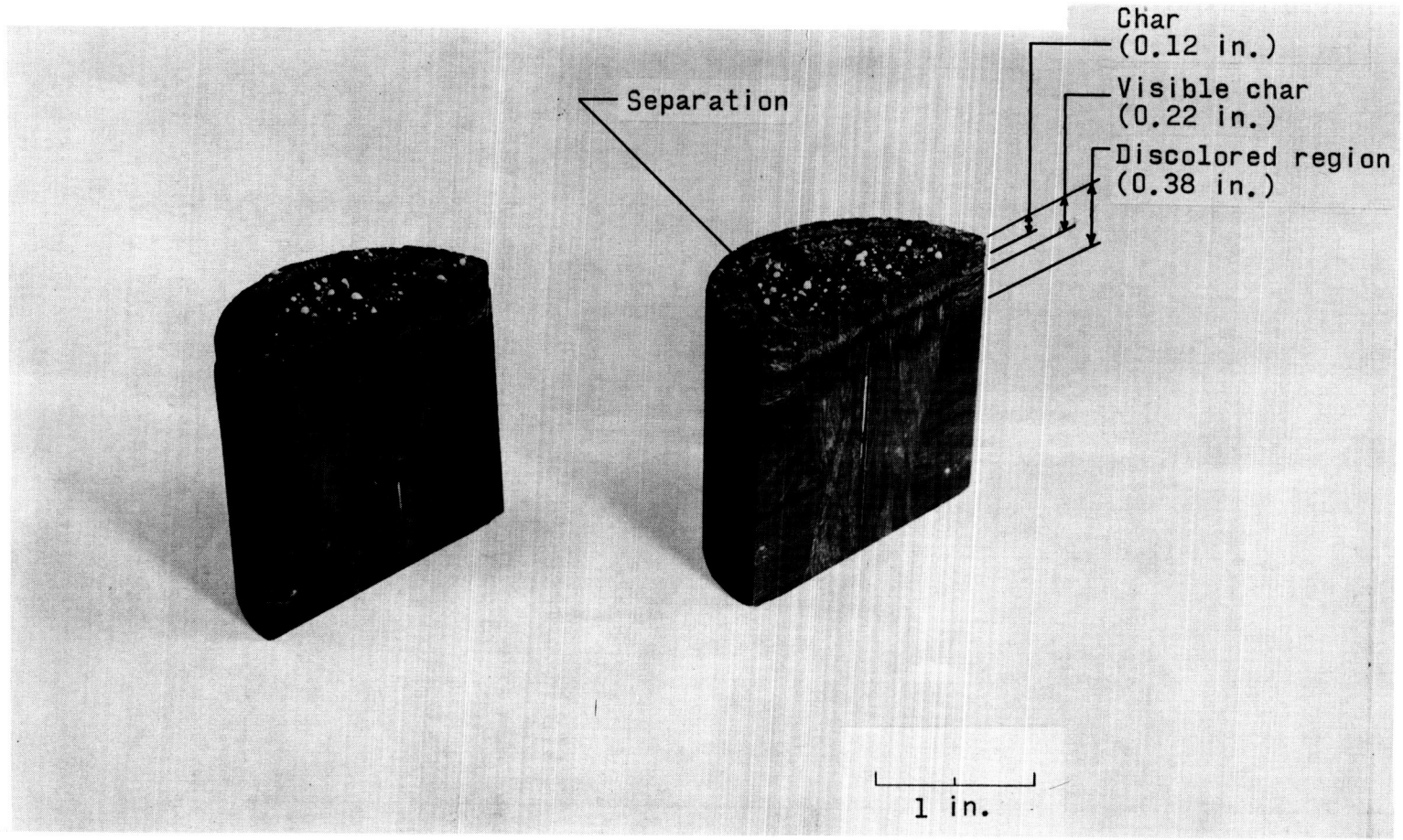

Figure 16.- Section of heat-shield center plug. G-60-2108

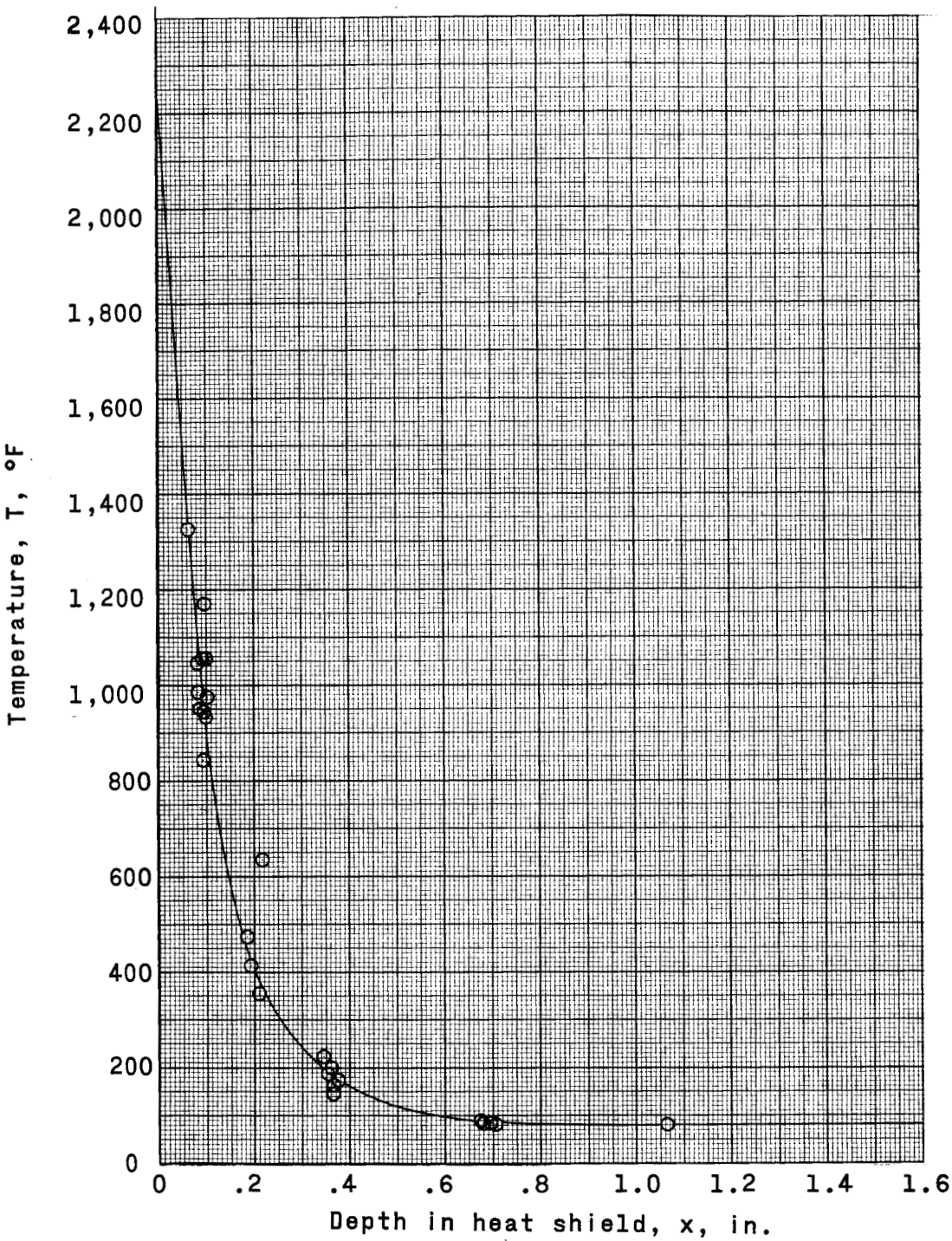

Figure 17.- Average temperature profile showing all sensor readings at t = 555 seconds.

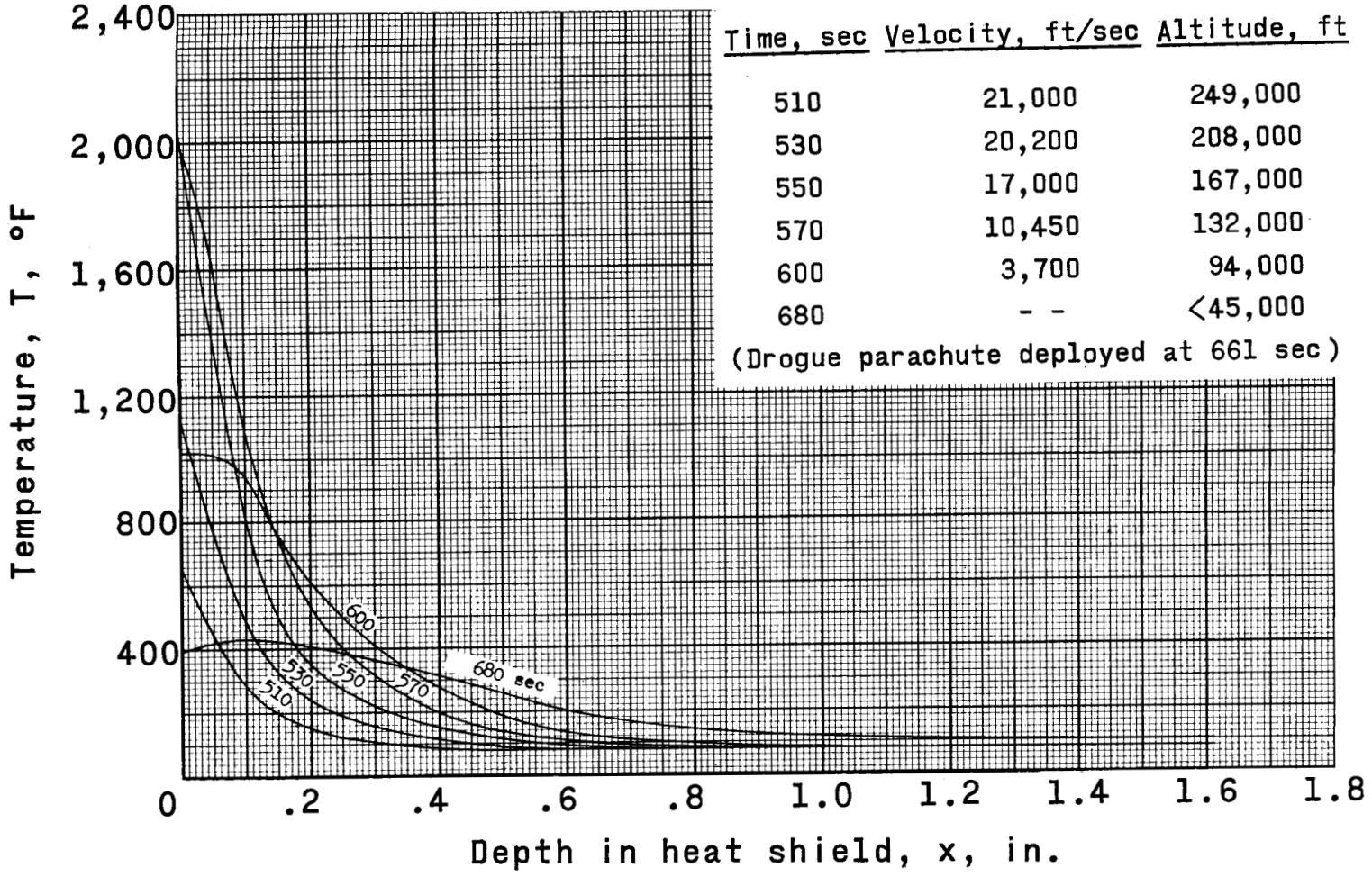

Figure 18.- Average temperature profiles existing at various times.

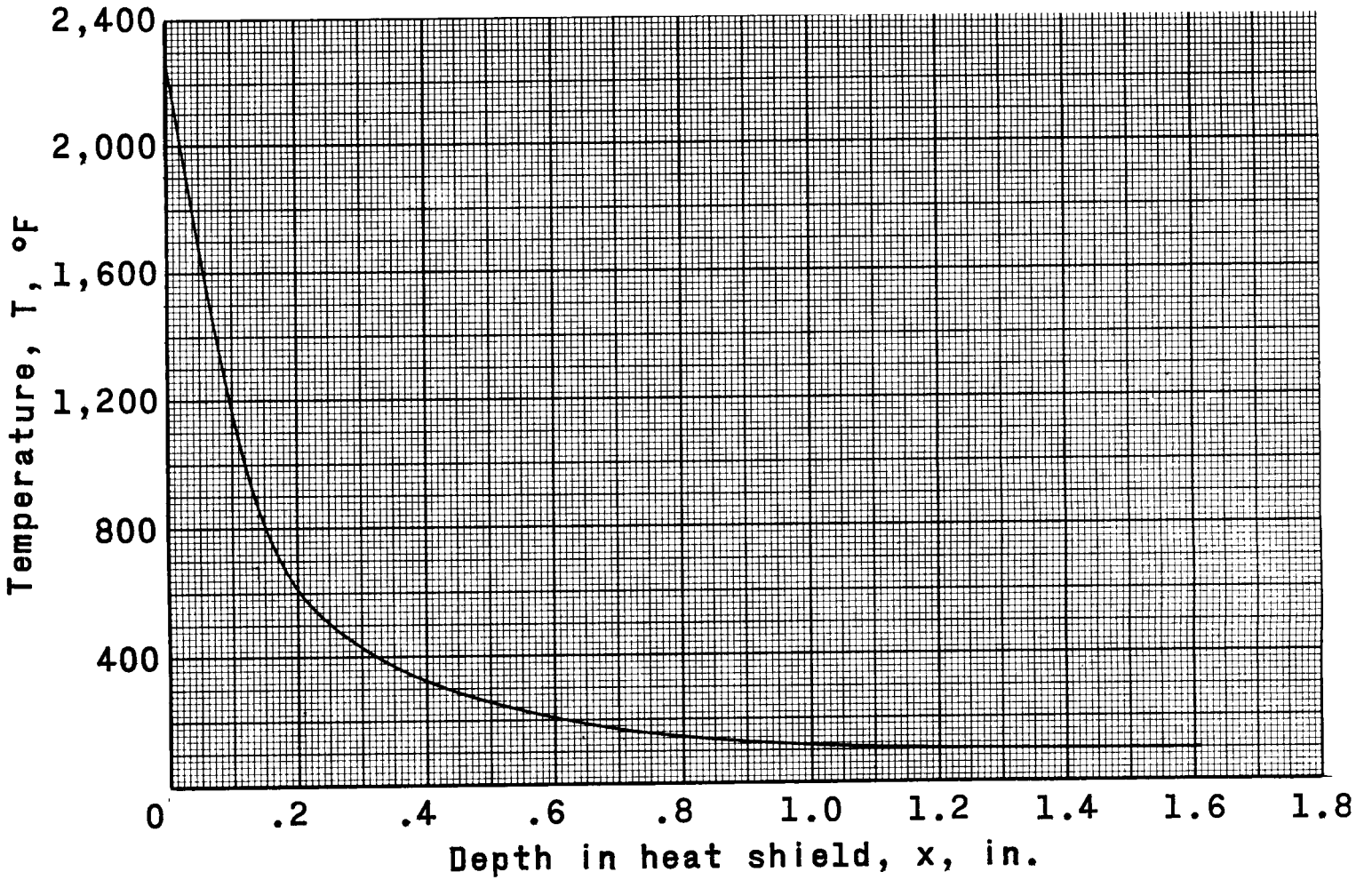

Figure 19.- Maximum temperature penetration by 680 seconds.

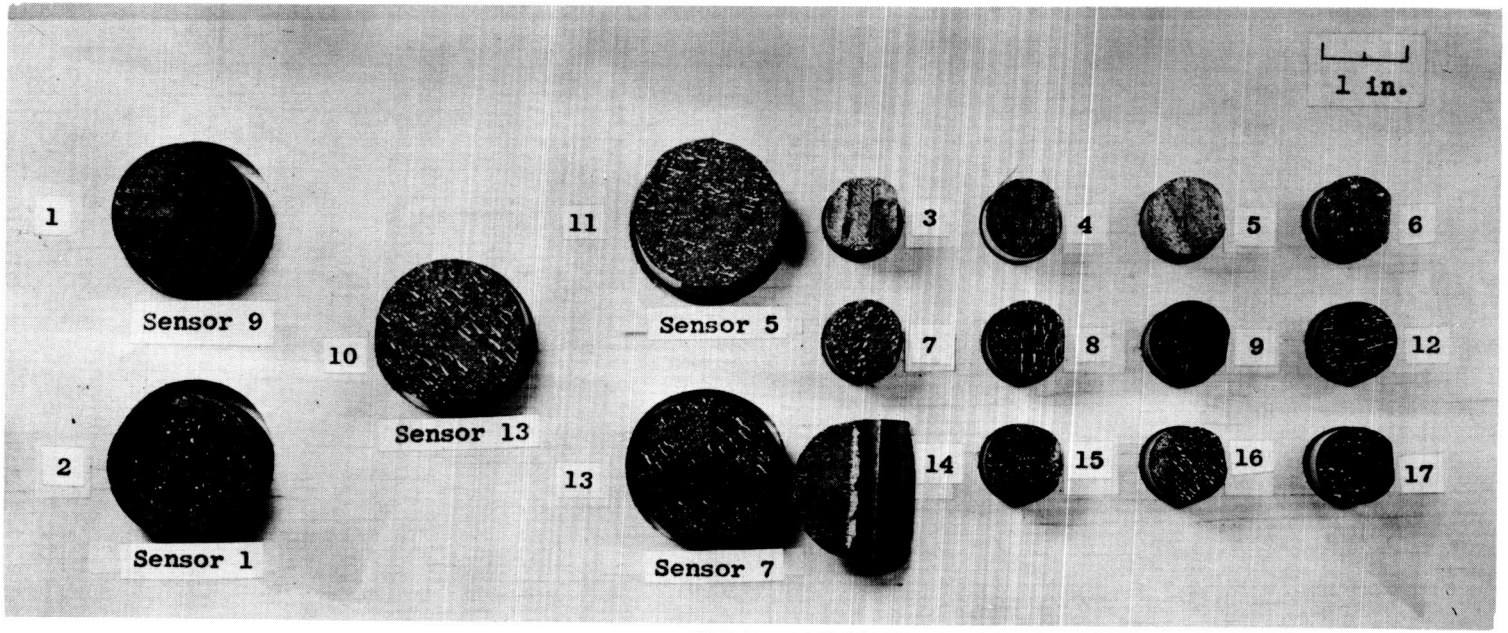

Figure 20.- Core samples obtained from recovered heat shield. G-60-2109

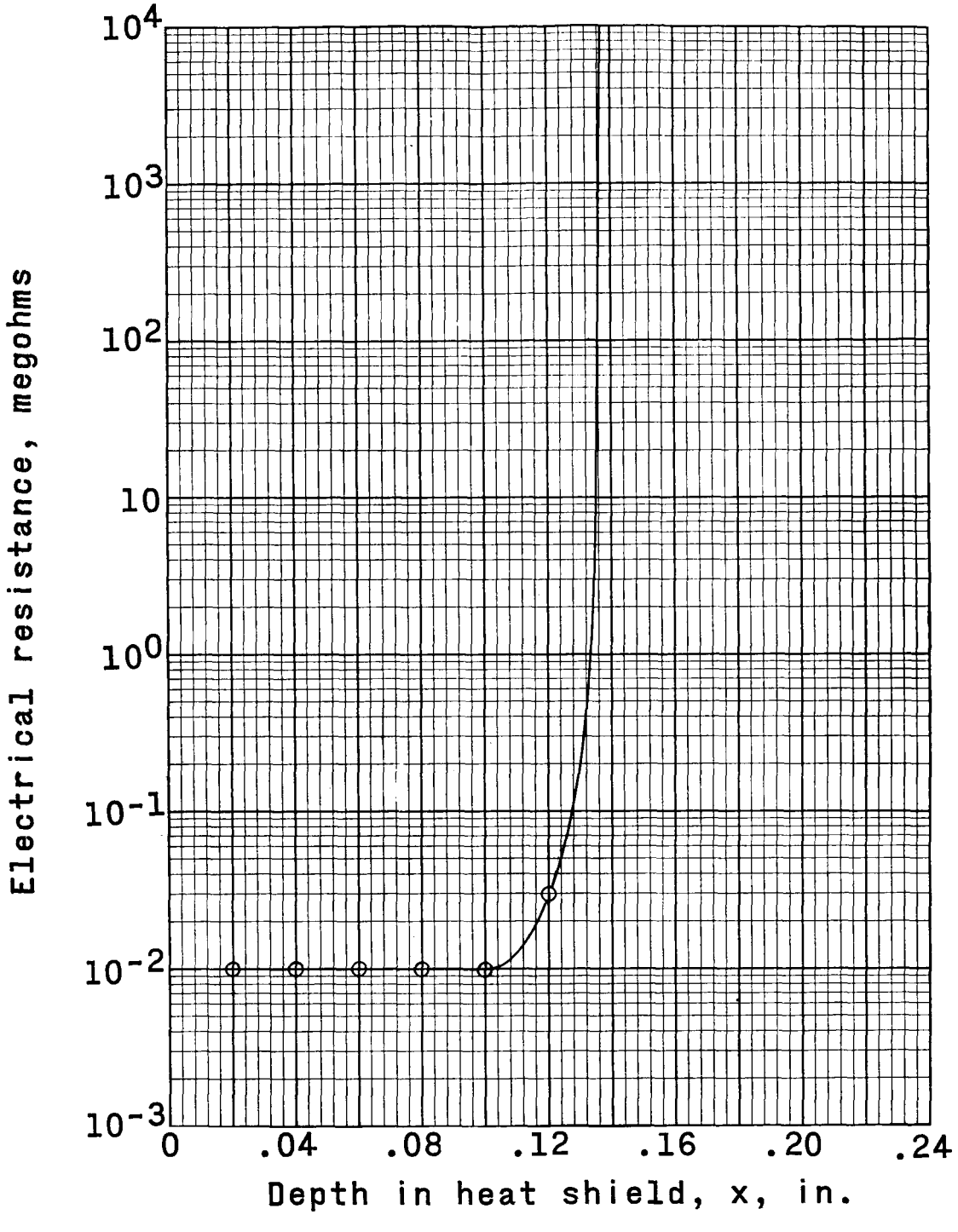

Figure 21.- Measured dielectric properties of recovered-heat-shield specimen. (Core sample 10.)

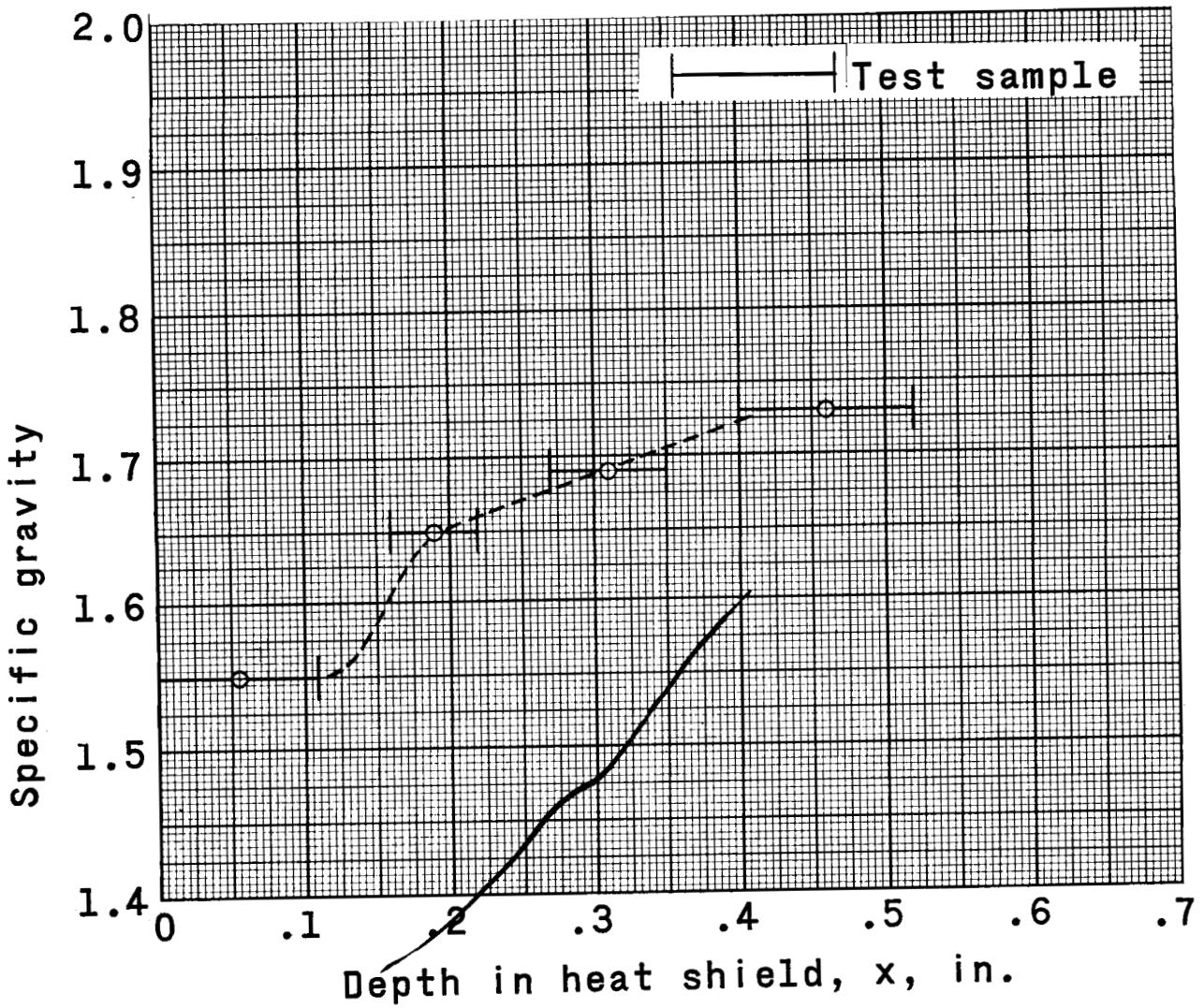

Figure 22.- Specific-gravity measurements of recovered-heat-shield specimens. (Core sample 13.)

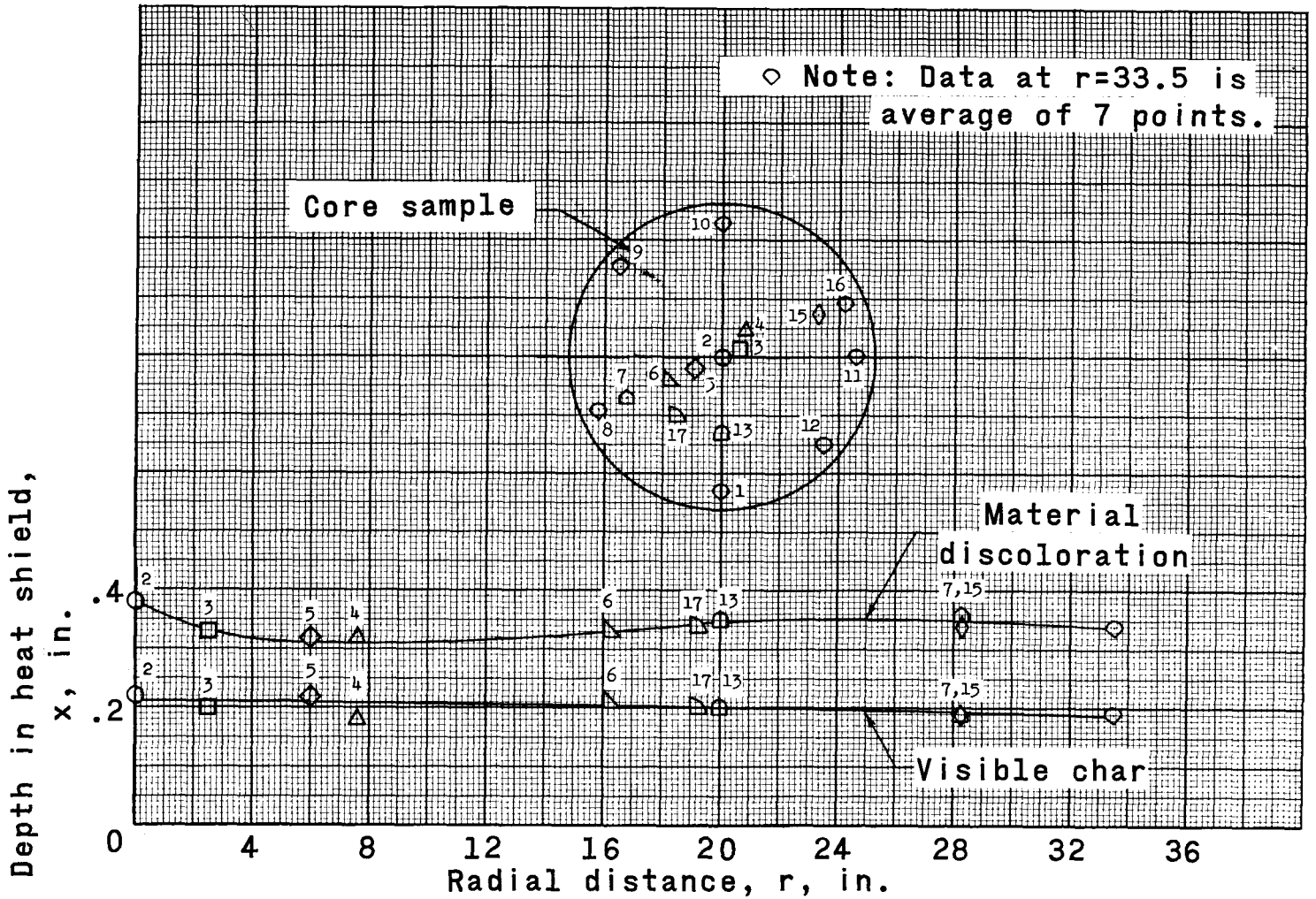

(a) Radial distribution.

Figure 23.- Visible-char and discoloration measurements on heat shield.

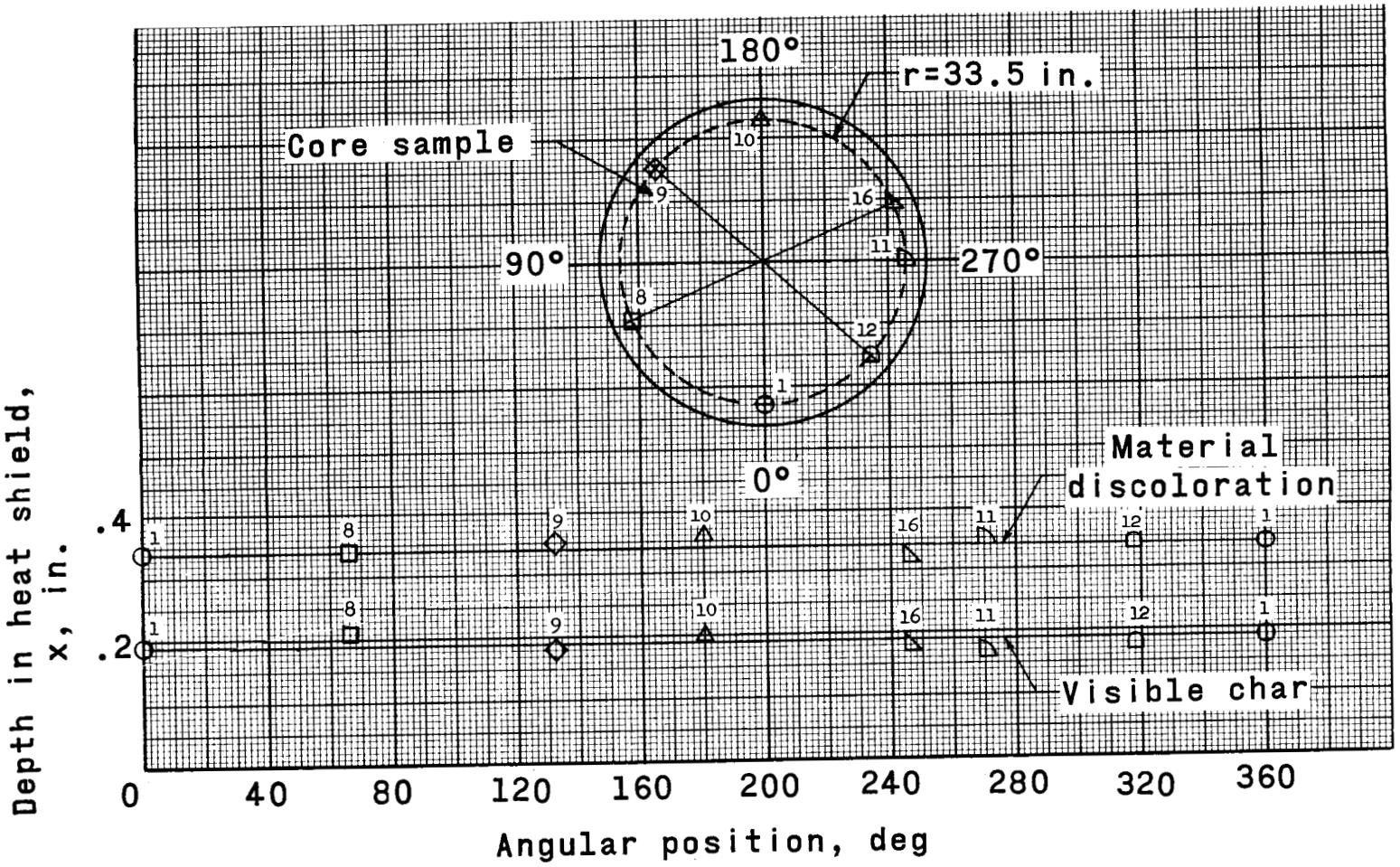

(b) Edge effect.

Figure 23.- Concluded.

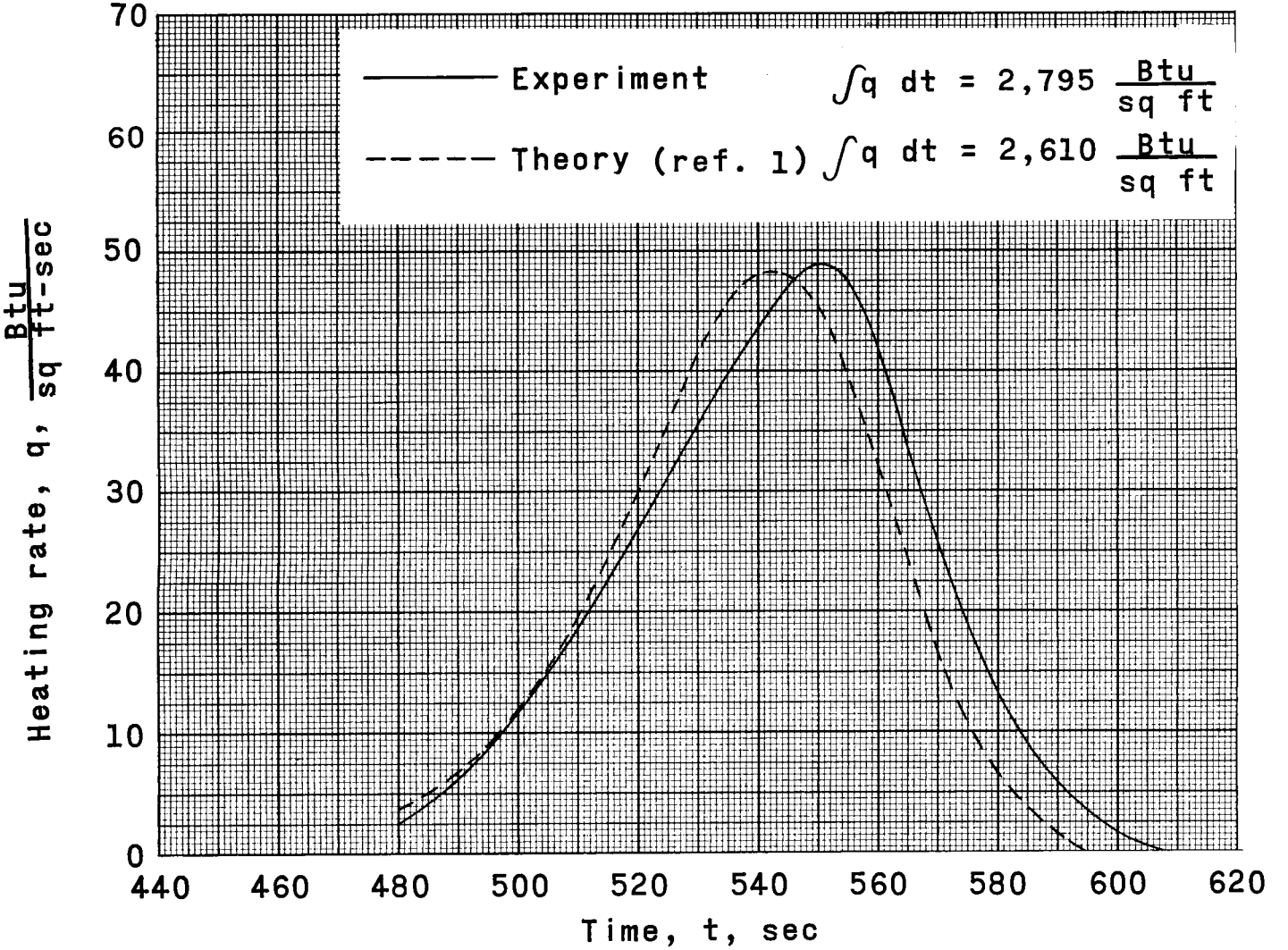

Figure 24.- Comparison of experimental and theoretical heating rate.

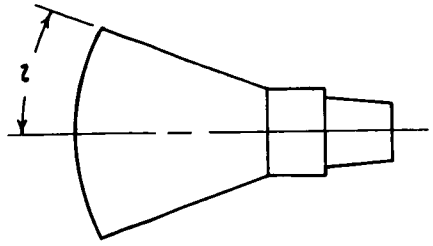

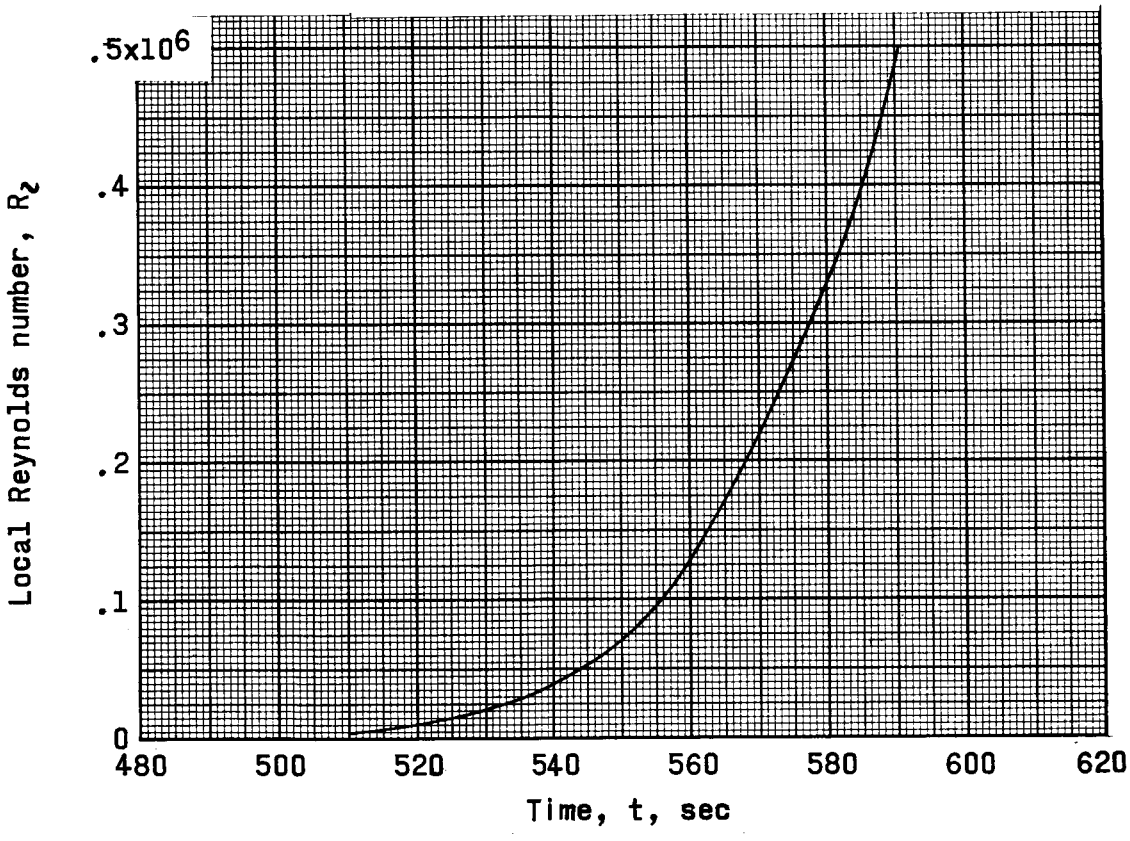

Figure 25.- Local Reynolds number at corner of heat shield. l = 3.23 feet.

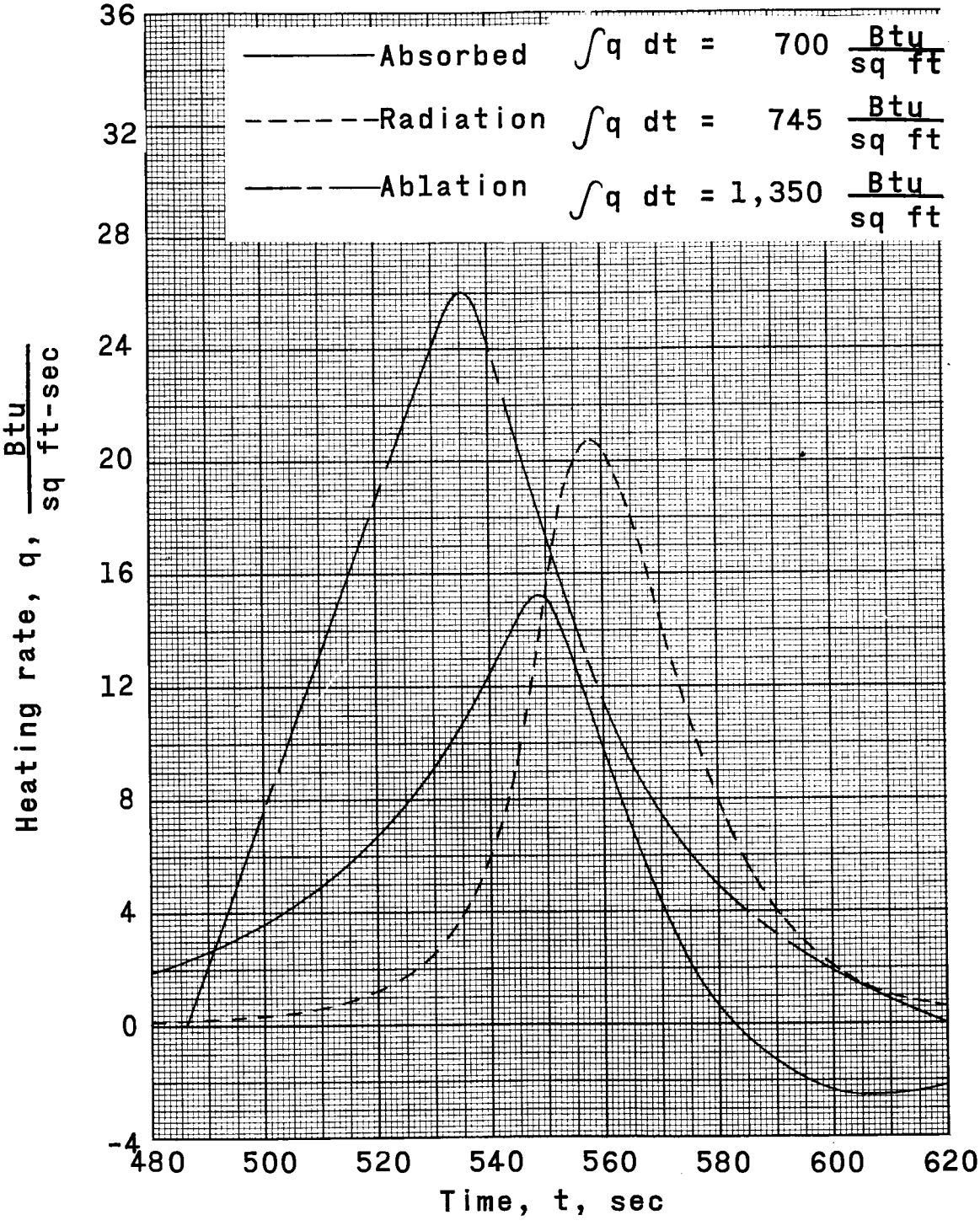

Figure 26.- Experimental values of potential heating rates.

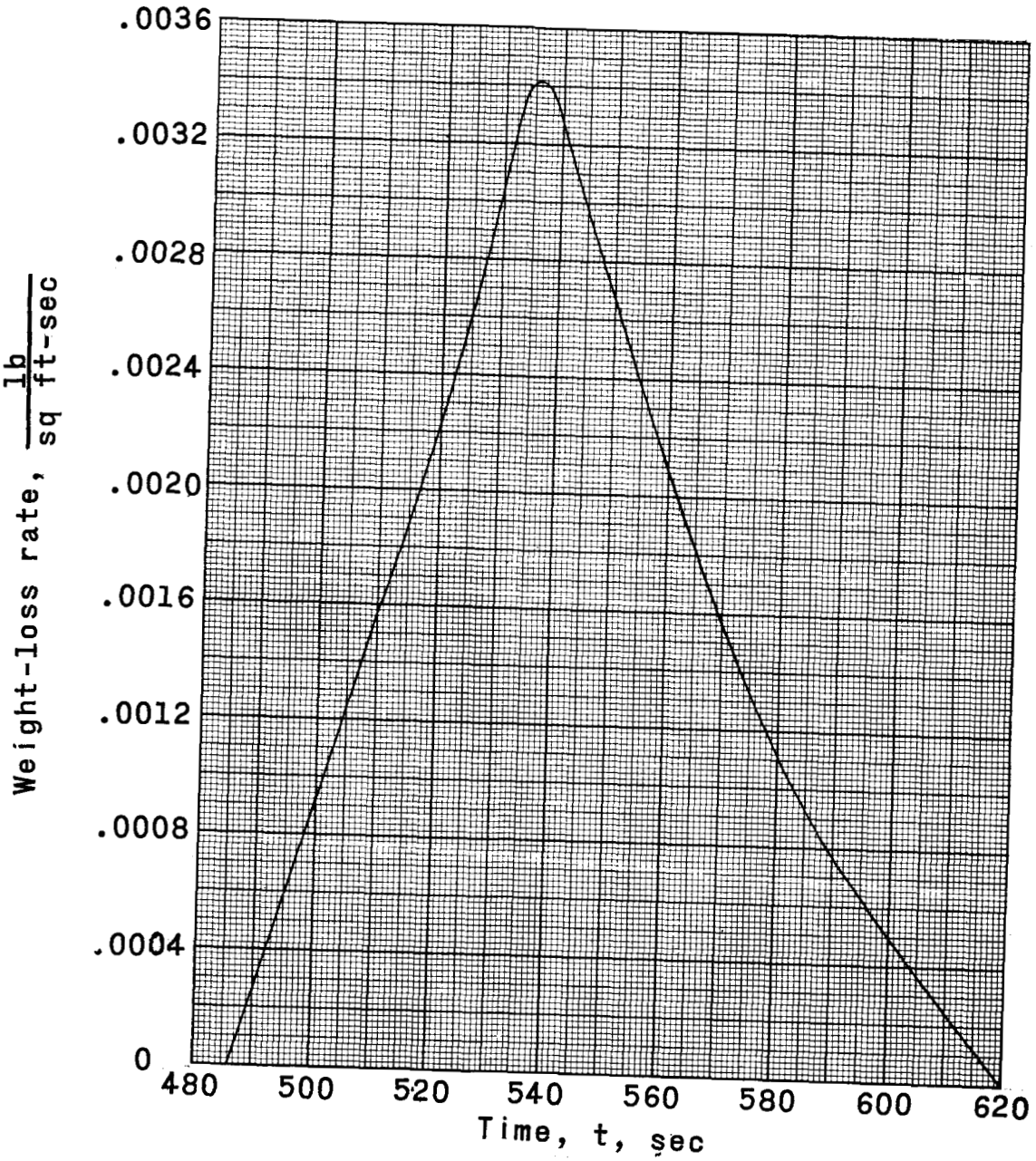

Figure 27.- Weight-loss rate of heat shield.

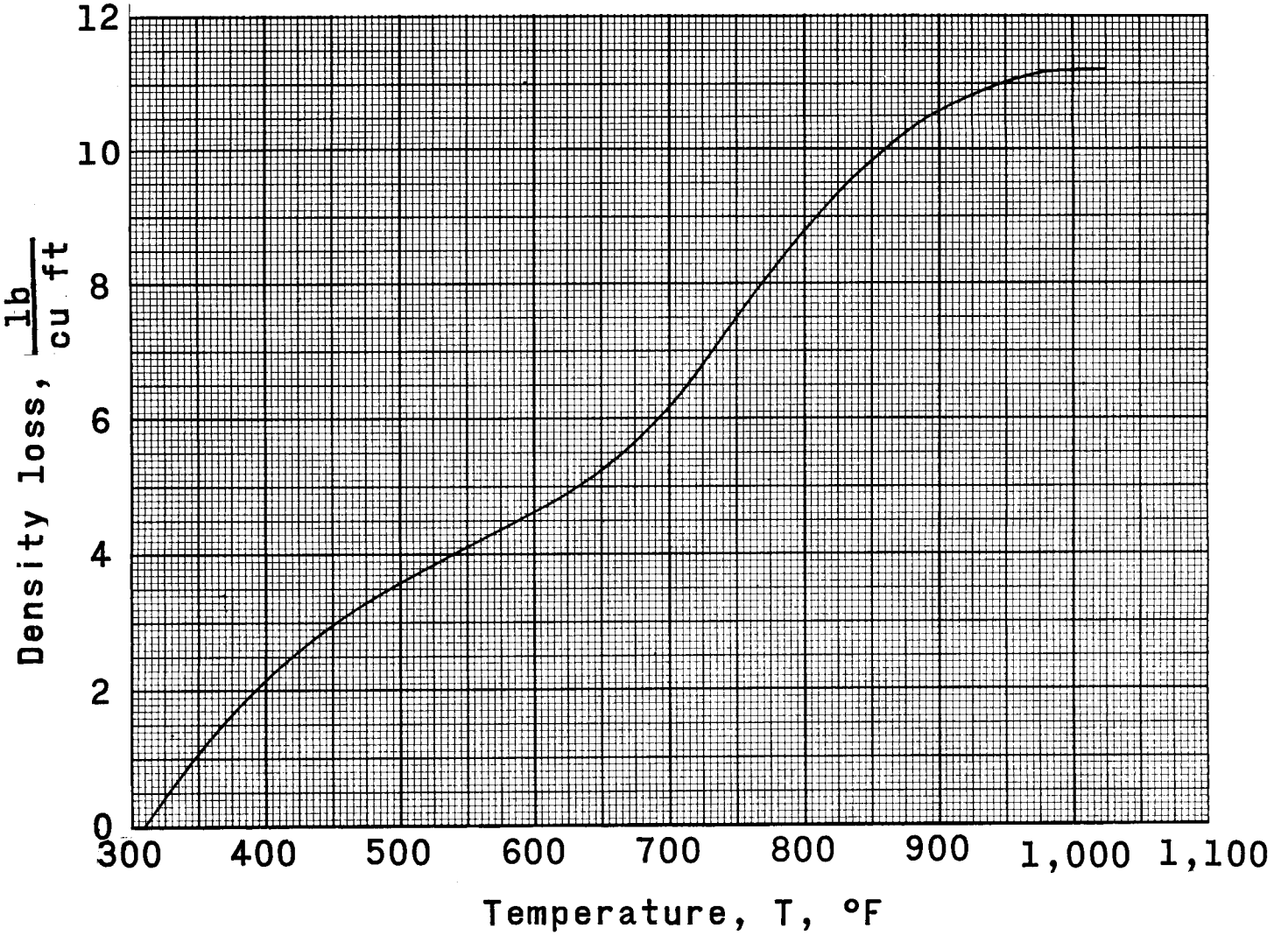

Figure 28.- Density loss variation with heat-shield temperature.

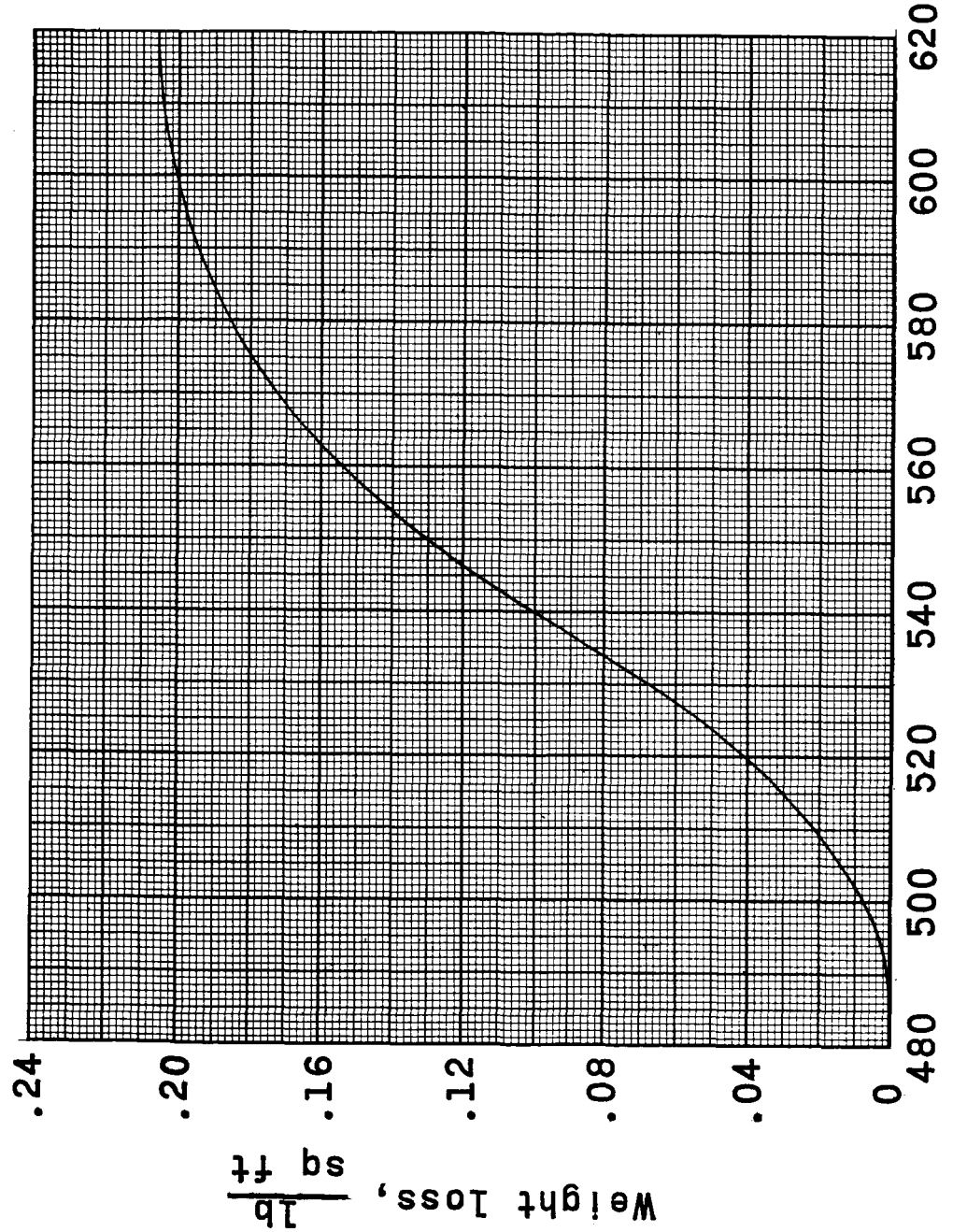

Figure 29.- Accumulative weight loss of heat shield.

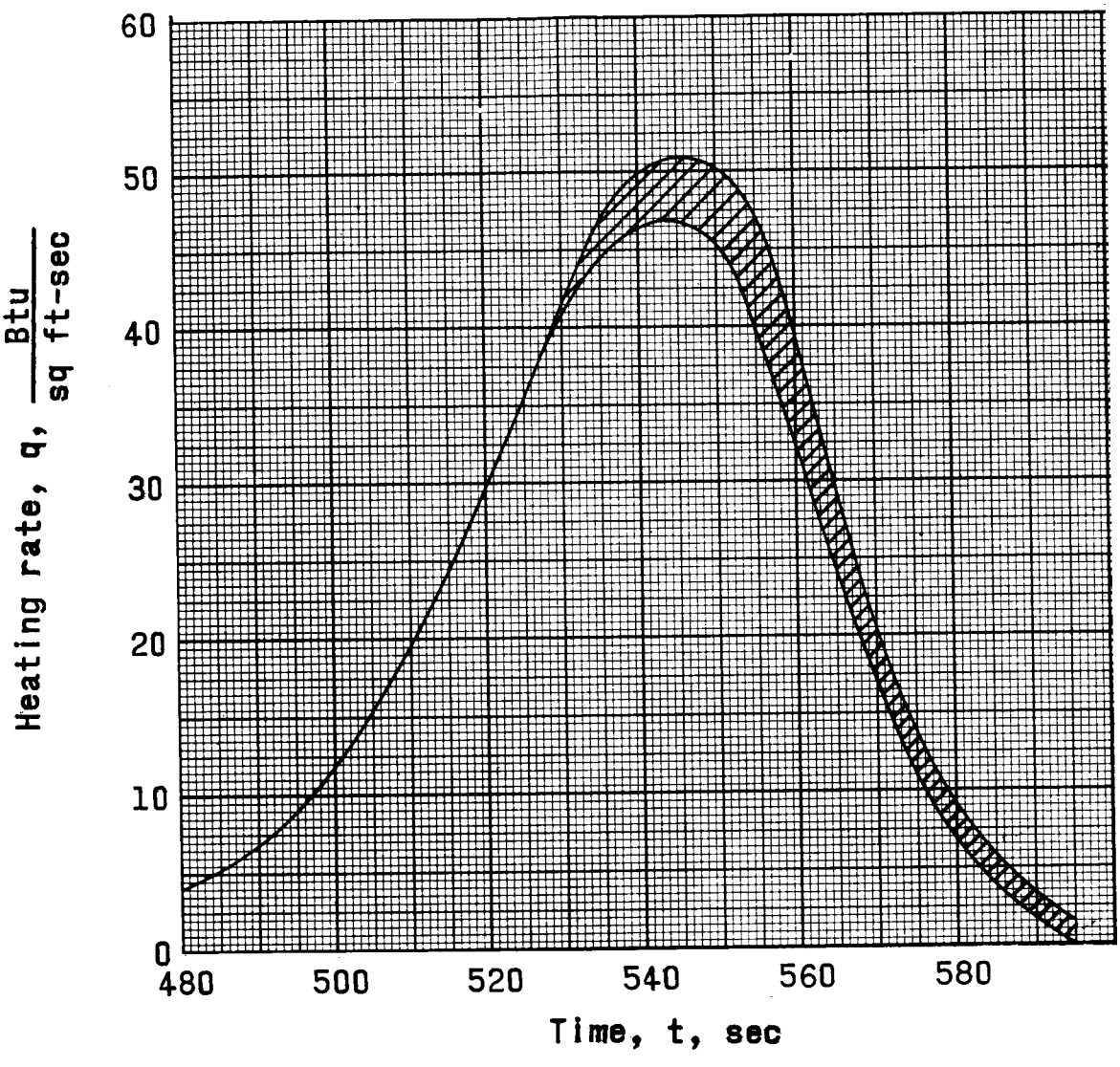

Figure 30.- Effect of atmospheric entry-trajectory uncertainties on stagnation-point heating rate.